Modeling the Distribution of Iron-oxides in Basalt by combining FIB-SEM and MicroCT Measurements

Frenk Out[1], Rosa A de Boer[1], John Walmsley[2], and Lennart Vincent de Groot[1]

[1]Utrecht University
[2]University of Cambridge

September 11, 2023

Abstract

Micromagnetic tomography (MMT) aims to go beyond paleomagnetic measurements on bulk samples by obtaining magnetic moments for individual iron-oxide grains present in a sample. To obtain accurate MMT results all magnetic sources and all their magnetic signals should be known. Small particles (<<1 μm) are often not detected by MicroCT analyses, but do have a magnetic signal, and therefore hamper obtaining reliable MMT results. Currently it is unknown how many of these small 'ghost grains' are present in basaltic samples. Here we aim to obtain a realistic grain-size distribution for iron-oxides in a typical Hawaiian basalt. We characterize the entire grain-size range of interest to paleomagnetism, from the superparamagnetic threshold of 40 nm to multidomain grains with sizes up to 10 μm. This requires a combination of FIB-SEM slice-and-view and MicroCT techniques: FIB-SEM characterizes the grains between 20 nm and 1 μm and MicroCT detects iron-oxides >750 nm. The FIB-SEM and MicroCT data are combined through normalizing the grain-size distribution using the surface area of non-magnetic minerals that are characterised in both datasets. Then, a lognormal-like grain-size distribution is acquired for the entire grain-size range. Our dataset enables future studies to populate (MMT) models with a realistic distribution of even the smallest iron-oxide grains, which ultimately may shed light on the confounding influence of such ghost grains on MMT results.

Modeling the Distribution of Iron-oxides in Basalt by combining FIB-SEM and MicroCT Measurements

Frenk Out[1], Rosa A. de Boer[1], John Walmsley[2], Lennart V. de Groot[1]

[1]Paleomagnetic laboratory Fort Hoofddijk, Department of Earth Sciences, Utrecht University, Budapestlaan 17, 3584 CD Utrecht, The Netherlands.

[2]Department of Materials Science & Metallurgy, University of Cambridge, 27 Charles Babbage Road, CB3 0FS Cambridge, United Kingdom.

Key Points:

- We produced a grain-size distribution of iron-oxides in a typical Hawaiian basalt from the superparamagnetic threshold (∼40 nm) to 10 micron
- We combined FIB-SEM and MicroCT data from sister specimens by normalizing them to the mineral surface area of the non-magnetic minerals
- Our grain-size distribution can be used to populate realistic models of iron-oxides in a Hawaiian basalt

Corresponding author: Frenk Out, `f.out@uu.nl`

Abstract

Micromagnetic tomography (MMT) aims to go beyond paleomagnetic measurements on bulk samples by obtaining magnetic moments for individual iron-oxide grains present in a sample. To obtain accurate MMT results all magnetic sources and all their magnetic signals should be known. Small particles (<<1 μm) are often not detected by MicroCT analyses, but do have a magnetic signal, and therefore hamper obtaining reliable MMT results. Currently it is unknown how many of these small 'ghost grains' are present in basaltic samples. Here we aim to obtain a realistic grain-size distribution for iron-oxides in a typical Hawaiian basalt. We characterize the entire grain-size range of interest to paleomagnetism, from the superparamagnetic threshold of ∼40 nm to multidomain grains with sizes up to 10 μm. This requires a combination of FIB-SEM slice-and-view and MicroCT techniques: FIB-SEM characterizes the grains between 20 nm and 1 μm and MicroCT detects iron-oxides >750 nm. The FIB-SEM and MicroCT data are combined through normalizing the grain-size distribution using the surface area of non-magnetic minerals that are characterised in both datasets. Then, a lognormal-like grain-size distribution is acquired for the entire grain-size range. Our dataset enables future studies to populate (MMT) models with a realistic distribution of even the smallest iron-oxide grains, which ultimately may shed light on the confounding influence of such ghost grains on MMT results.

Plain Language Summary

Micromagnetic tomography (MMT) is a promising new technique that extracts high-quality magnetic information from lavas. Magnetic particles in lavas obtain a magnetic signal while cooling in presence of Earth's magnetic field. However, not all particles store the signal well, meaning that both good and bad recorders are present. Classical paleomagnetic techniques measure the magnetic signal of all recorders together, i.e. the bulk signal. MMT, however, acquires the signal from individual recorders in the lava, enabling selecting only the good recorders and rejecting the signal of bad recorders. MMT needs two pieces of information: (1) the surface magnetic field produced by recorders and (2) the location of all recorders in the lava. Unfortunately, the position of recorders smaller than ∼1 μm are often unknown due to measurement limitations. If these small particles are not detected, they may scramble the calculated signal of larger recorders. To investigate how many disruptive undetected grains are present, we scanned a small vol-

ume of lava on high resolution to extract all magnetic recorders and obtain a grain-size distribution. With this distribution we may estimate if these small recorders distort the signal of larger detected grains.

1 Introduction

Volcanic rocks are often perceived to be excellent recorders of paleomagnetic fields, although only a small portion of all minerals in a volcanic rock has magnetic properties. These minerals, iron-oxide grains, present in a lava acquire a magnetization by cooling in the Earth's magnetic field. Their magnetization is thus a thermo-remanent magnetization (TRM), and these magnetic signals are regarded to be stable, often over millions or billions of years (e.g. Dunlop & Özdemir, 1997; Tauxe & Yamazaki, 2015).

Small particles, or single domain (SD) grains, have two configurations for storing their magnetic signal: either parallel or anti-parallel to the grain's easy axis. One of these two options is selected at random but with a slight preference to align with the prevailing magnetic field (e.g. Tauxe, 2010; Berndt et al., 2016). In slightly larger particles, which are often referred to as pseudo-single domain (PSD) grains, the magnetic signal is stored in a more complex vortex structure. Fortunately, this signal usually represents the original imparting magnetic field accurately (Nagy et al., 2017). The last group of particles are iron-oxides with diameters >1 μm and belong to the multi-domain (MD) class. Although these MD grains may store magnetic signals for millions of years, their expression of the past field is often disturbed, overprinted, unstable, or lost (e.g. De Groot et al., 2014). This instability is caused by magnetic reassembling of the original magnetic structure of a grain over time to achieve energy minimization (Néel, 1955). MD grains are therefore mostly perceived as bad paleomagnetic recorders, while SD and PSD grains are considered to be more reliable recorders of paleomagnetic fields. To make it even more difficult, most natural rock samples consist of a mixture of SD, PSD and MD grains. The combination of these good and bad recorders in rocks is the main reason that generally only 10 to 20% of all paleointensity experiments pass sufficient selection criteria to yield usable results (e.g. Tauxe & Yamazaki, 2015; Nagy et al., 2017).

To circumvent the problem of acquiring signals simultaneously from good and bad recorders, de Groot et al. (2018) proposed a new paleomagnetic technique to obtain magnetic moments of individual iron-oxide grains in a sample: micromagnetic tomography (MMT). MMT infers magnetic moments by first acquiring a magnetic surface image of a (cut-out of a) thin-section of a sample using a surface magnetometry technique (e.g. a Quantum Diamond Microscope: Glenn et al., 2017). Then, the position of each iron-oxide grain in that sample is obtained with X-Ray micro computed tomography (MicroCT).

These two pieces of information are combined in a mathematical inversion to retrieve individual magnetic moments by minimizing residuals in the magnetic surface map. Both de Groot et al. (2021) and Kosters et al. (2023) have shown the capabilities of MMT on Hawaiian rock samples. The mathematical uncertainties of the technique have been modeled in Out et al. (2022).

Theoretically, MMT is able to retrieve the magnetic moment of even the smallest SD iron-oxide particles. These particles are unfortunately often not detected by present-day MicroCT equipment, because these machines have resolutions down to 350-500 nm. As a grain can only be reliably resolved if it consists of a couple of voxels, it is only possible to detect particles with a diameter of >1 μm. Consequently, SD and PSD particles may produce a detectable magnetic signal in the magnetic surface scan, while they do not show up in the MicroCT data. This problem challenges MMT, because the method can only deliver unique and reliable results if all measured magnetic signals originate from detected iron-oxides in the sample (Fabian & De Groot, 2019). Currently it is unknown how many small iron-oxides that go undetected by the MicroCT analyses (i.e. ghost particles) are present in (Hawaiian) basaltic lavas. Here we aim to image and characterize the distribution of these ghost particles using Focused Ion Beam Scanning Electron Microscopy (FIB-SEM), following the slice-and-view approach of Nikolaisen et al. (2020). With FIB-SEM it is possible to image a sample of micrometer size with a resolution of $\sim$20 nm by slicing (or milling) through the sample and imaging the cleared surface. In this way, a 3D reconstruction of the sample volume with these previous undetected iron-oxide particles can be reconstructed. Since iron-oxide grains reflect electrons well, the particles are simply detected through backscattered electron images obtained with scanning electron microscopy. Nikolaisen et al. (2020) used the grain shapes to model micromagnetic properties of the individual grains that were characterized by the FIB-SEM analyses. Here we will use the three dimensional characterisation of the small iron-oxides present in our sample to reconstruct a grain-size distribution. We combine the grain-size distribution obtained using the FIB-SEM with the MicroCT analyses on the same sample material to obtain a grain-size distribution spanning both the nanometer and micrometer scale. Linking these two datasets, however, is not straightforward because iron-oxides are not uniformly present in a rock sample but cluster around large mineral interfaces. We therefore use the surface area of relatively large, non-magnetic, grains in both the FIB-SEM and MicroCT data to normalize and combine the grain-size distributions ob-

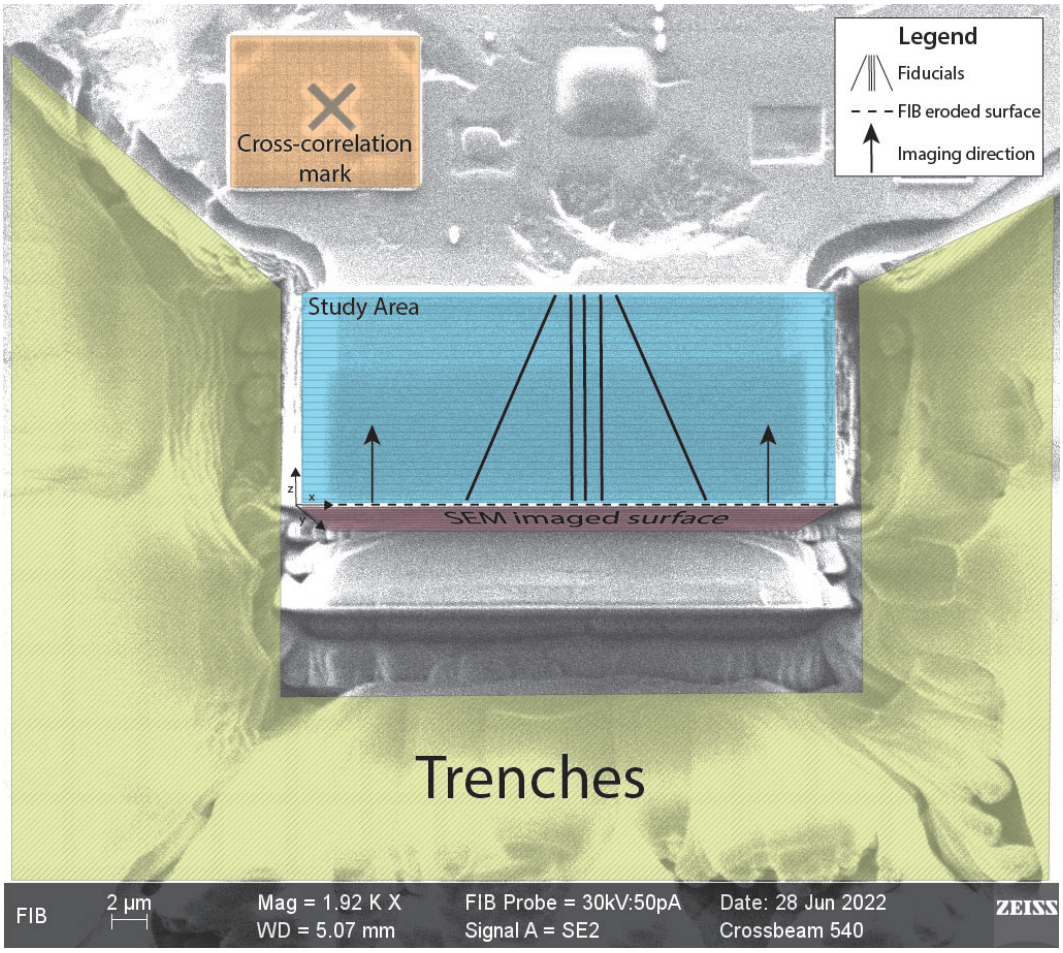

Figure 1. Overview of the study area within a Hawaiian basalt examined by slice-and-view through FIB-SEM. After the ion beam removed a 20.18 nm slice from the bottom of the study area, a backscattered and secondary reflected electron image is recorded. Instrumental drift is constrained by calibrating the FIB-SEM every 100 slices using the cross-correlation mark in the top left corner.

tained from both analyses. Lastly, we will demonstrate how these particles can be placed in numerical models to simulate a realistic basalt sample. With these models, it might ultimately be possible to investigate the effect of resolution limitations of MicroCT leading to the presence of ghost particles in MMT analyses.

2 Grain-size distribution

Pivotal in obtaining a realistic grain-size distribution is acquiring dimensional properties of all iron-oxide grains present in basaltic rocks. The sample we have used in this

study was taken from the 1907 lava flow from Hawaii (HW-03; de Groot et al., 2013; ter Maat et al., 2018)). The MicroCT data of this sample had already been studied by de Groot et al. (2021) and Kosters et al. (2023), facilitating the detection of grains larger than ∼1 μm, but leaving most of the SD and PSD particles undetected. Fortunately, with the help of FIB-SEM (e.g. Einsle et al., 2016; Nikolaisen et al., 2020) these remaining SD and PSD grains could finally be made visible. FIB-SEM allows a pixel size of 10 nm and a field of view close to 20 by 20 μm, which enables the detection of both the smallest SD grains above the superparamagnetic threshold of 40 nm (Dunlop & Özdemir, 1997) and large MD grains of >1 μm, which are normally at the lower detection limit of MicroCT.

2.1 Image acquisition with FIB-SEM

We applied FIB-SEM on a sample of HW-03, following the slice-and-view procedure described in Einsle et al. (2016) and Nikolaisen et al. (2020). A 60 μm thick slice with a diameter of 2 mm was extracted from the specimen and coated with a nanometer thick layer of gold. Around the edges of the sample, silver was applied with a toothpick so that electrons could easily pass through the sample. The sample was placed in a Zeiss Crossbeam 540 after which we searched the top of the sample for a 20 x 20 μm area containing many small iron-oxides. This area was prepared for the slice-and-view procedure by first applying a 1 μm thick layer of platinum while maintaining an ion beam current of 700 pA and an accelerating voltage of 30 kV. This accelerating voltage did not change unless explicitly stated otherwise.

Then, five 0.5 µm deep fiducials were engraved with a current of 50 pA (Fig. 1). The three central fiducials were created parallel to each other to enable image alignment during data processing. The outer two fiducials were created under an angle of 25 degrees with respect to the three central fiducials. These two fiducials ensured that the real thickness of the individual image slices could later be checked. To make these fiducials visible, a 0.6 μm thick carbon layer was deposited on top of the platinum layer with an ion beam current of 700 pA and a dwell-time of 400 seconds. Then, three trenches with a depth of 25 μm and an area of 27 by 46 μm^2 were eroded at three sides of the selected area. For this erosion procedure, we used an ion beam current kept at 15 nA with a back-and-forth milling pattern (bidirectional). Using the same bidirectional routine, the current was reduced from 15 nA to 7 nA to create smooth trenches next to the studied area.

Instrumental drift during measurements was reduced to a minimum by applying a cross-correlation mark outside the studied area (Fig. 1).

The data acquisition process was initiated after a 20.18 nm slice of the sample area was removed with FIB (beam current at 1.5 nA with an accelerating voltage between 1 to 6 kV). Backscattered and secondary reflected electrons images where obtained using SEM, after which a 20.18 nm layer of sample was removed using FIB. After this procedure was repeated a hundred times instrumental drift was corrected by checking alignment with the cross-correlation mark. The entire process was finished in one day, in which 601 grayscale images of both backscattered and secondary reflected electrons were saved in TIFF format. Each file encompassed a pixel area of 3072 x 2104 pixels with a pixel size of 10.09 nm and a 8-bit grayscale. The total volume of sample analysed was therefore 31.0 x 21.2 x 12.1 μm^3.

2.2 Dataprocessing

2.2.1 Extracting particles from FIB-SEM data

After image acquisition, a grain-size distribution could be extracted from the data. Every data processing step was executed with Python 3 and the OpenCV library (Bradski, 2000). We initiated our data processing by loading the 601 backscattered electron images and aligning them using the three parallel fiducials and the matchTemplate function of OpenCV. After alignment, we removed all duplicate images. To remove the effects of both curtaining and the platina and carbon deposited layers, every image was cropped to 2600 $\times$ 1000 pixels.

Through denoising and thresholding, SD and PSD iron-oxides could be extracted from FIB-SEM images as shown by Nikolaisen et al. (2020). However, we designed the extraction process in such a way that both the surface and the centre of each iron-oxide grain were properly retrieved. We initiated denoising by 2$\times$2 binning of the 549 remaining images, which resulted into 1300 $\times$ 500 pixels per image. A non-local means denoising filter from OpenCV (`fastNlMeansDenoisingMulti`) was used with a search windowsize of 20 pixels, a filter strength of 20, and template windowsize of 3 pixels applied in the x, y, and z-direction. Each image was then thresholded at a pixelvalue of 220. After thresholding, all images are stacked together into one 3D-volume. In this 3D-volume,

we grouped connected pixels into grains. With this high threshold, we have only obtained the brightest central iron-oxide pixels.

However, the iron-oxide grains are not properly imaged yet, because the sides of the grains frequently have a lower pixel value than their center and thus have dropped out in the previous thresholding step. To correctly image the boundary of the iron-oxides we applied a lower threshold value of 160 instead of 220 to the previous set of images. Then we applied the canny edge algorithm of OpenCV (`Canny`). This algorithm detects spatial changes in pixel value and draws, based on that change, boundaries between pixel values. After drawing boundaries, small gaps in the boundaries were closed using the morphology close operation in order to create enclosed areas. Again, all images were combined into a 3D-volume and connected pixels were grouped into grains. However, the low threshold outputted both well defined grain shapes of iron-oxides and poorly defined shapes of other unwanted minerals. To get rid of these unwanted minerals, we mapped the grains obtained with high thresholding (poorly defined boundaries, most certainly iron-oxides) on top of the grains obtained with low thresholding (well defined boundaries, possible iron-oxides) to only remain with actual iron-oxides. Lastly, we removed all iron-oxides that extend beyond the edges of the FIB-SEM domain. We calculated the volume of 1,558 remaining iron-oxides, and transformed these volumes into an equivalent diameter assuming spherical grains.

2.2.2 Scaling FIB-SEM and MicroCT data

To obtain a grain-size distribution spanning the entire range of naturally occurring iron-oxides, we combined our FIB-SEM data with MicroCT data that was obtained on a sister specimen of HW-03 by Kosters et al. (2023). Since iron-oxides are not homogeneously distributed throughout the rock, it is not straightforward to link MicroCT data one-to-one to FIB-SEM data based on volume. Most iron-oxides are positioned on the interface between larger grains (mainly plagioclase and pyroxene); especially the smallest iron-oxides attach themselves to this 'honeycomb' structure of other minerals (Fig. 2). Because this honeycomb structure of relatively large minerals can be imaged properly using MicroCT, it allows for extrapolating the number of undetected small iron-oxides from the FIB-SEM analysis to the MicroCT data and hence produce a continuous grain-size distribution over both analyses.

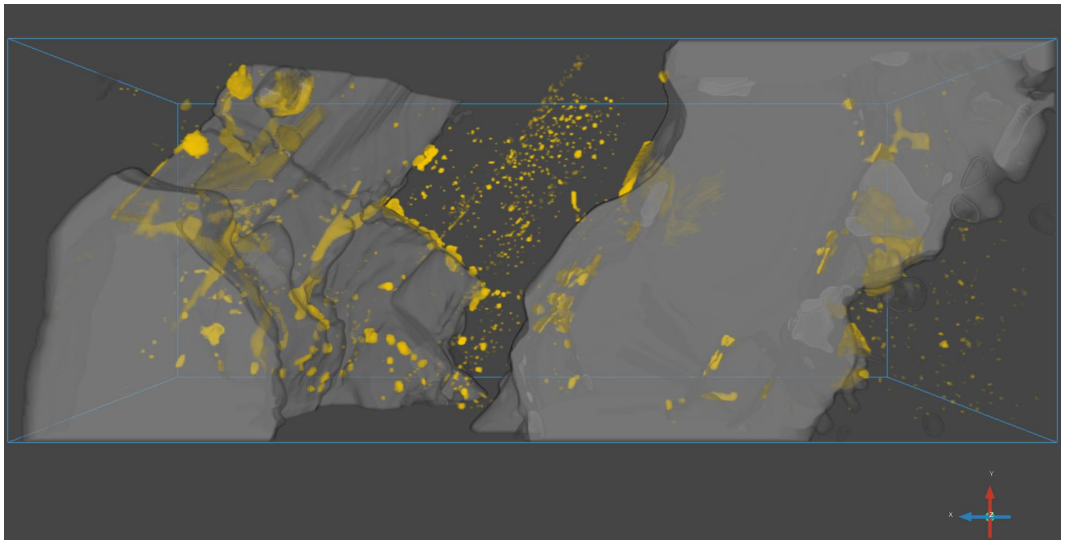

Figure 2. Overview of the 26.2 × 10.1 × 10.5 μm^3 volume exposed to the slice-and-view procedure with FIB-SEM. The large grains are indicated by a grayish color. The iron-oxides residing in this volume are indicated in yellow-brown. Note that most iron-oxides reside on the large mineral interfaces.

Characterizing the mineral surface area of the larger minerals, mainly plagioclase and pyroxene, required reprocessing the FIB-SEM data, with this specific goal in mind. First, the FIB-SEM dataset was denoised using a non-local means filter; then we applied a median filter with a spherical footprint of 13 pixels in diameter to smooth out irregularities at the boundaries. After this pre-processing we applied a K-means algorithm to create five groups of pixels. For each individual image, we removed the first group because it corresponded to drilling artifacts. Additionally, we removed all areas smaller than 3000 pixels, because these areas do not represent grain interfaces of the larger minerals present in the sample that are typically occupied by iron-oxides. Finally, the mineral surface area was calculated for the remaining pixel values using a 'Lindblad' algorithm (Lindblad, 2005). The mineral surface area consisted of about 3.8 × 10^6 squared pixels that correspond to an area of 1.53 × 10^{-3} mm^2. Fig. 2 shows the position of the mineral surface area together with the iron-oxides.

To calculate the mineral surface area in the MicroCT dataset, we started with raw MicroCT data and processed it using Dragonfly software. After loading the DICOM files, we cropped about 100 μm on both sides of the sample to remove scanning residuals. To align the sample with the coordinate axes, we rotated the sample 0.85° clockwise around

the z-axis, 0.50° anticlockwise around the x-axis, and resampled the image with 0.75 μm pixel size. Then the image was cropped further, which resulted into a region of 1979 × 44 × 1901 voxels. We denoised the image by applying a non-local means filter with a 3D spherical kernel size of 11 pixels. To create a larger contrast we applied a median filter with a 3D spherical kernel size of 13 pixels. The different minerals were separated by applying a K-means filter of 3 groups, of which the group with the highest pixel value corresponds to iron-oxides. The other two groups chiefly consisted of plagioclase and pyroxene. Since we observed that SD and PSD iron-oxides tend to cluster on the interfaces of these minerals, we applied a 'sobel edge detection' filter to these groups. The result of this filter enabled us to create a honeycomb structure of the sample, on which we could populate SD and PSD iron-oxides to create realistic models of basalts. This mineral surface area of 4.00 mm^2 is approximately 2,620 times larger than the surface area found in the FIB-SEM dataset. This means that we need to multiply the number of FIB-SEM grains by 2,620 to scale correctly to the MicroCT dataset. This resulted into a combined dataset of 4.7 $\times 10^6$ FIB-SEM and 1.6 $\times 10^3$ MicroCT iron-oxide grains. The FIB-SEM and MicroCT datasets can now be combined to produce a continuous grain-size distribution of iron-oxides for the entire range of interest (Fig. 3). The median grain-size has a diameter of 70 nm. From 30 to 70 nm the occurrence rapidly increases, after which the occurrence of grain diameters between 70 nm and 10 μm follows are more gradually decaying trend.

2.3 Constructing the grain-size distribution

The trend in grain-size distribution can be described using a lognormal-like distribution between 20 nm and 10 μm. We have chosen the lognormal distribution, because this distribution is frequently used to describe grain-sizes for e.g. magnetite powders (Smirnov, 2006; Yu et al., 2002). Nevertheless, the lognormal trend line was originally fitted to the 10^{th}-logarithm of the data. This logarithm ensures a better fit to grain-sizes larger than 70 nm. Through an iterative procedure reducing the least-squares error of our fit to the data, we found the best fitting distribution after which we transformed it back to linear space:

$$p = 3.51 * 10^{-6+\frac{5.61}{d\sqrt{2\pi}}e^{-\frac{\ln^2(0.60d)}{6.29}}} \text{ if } d : [0, 10] \quad (1)$$

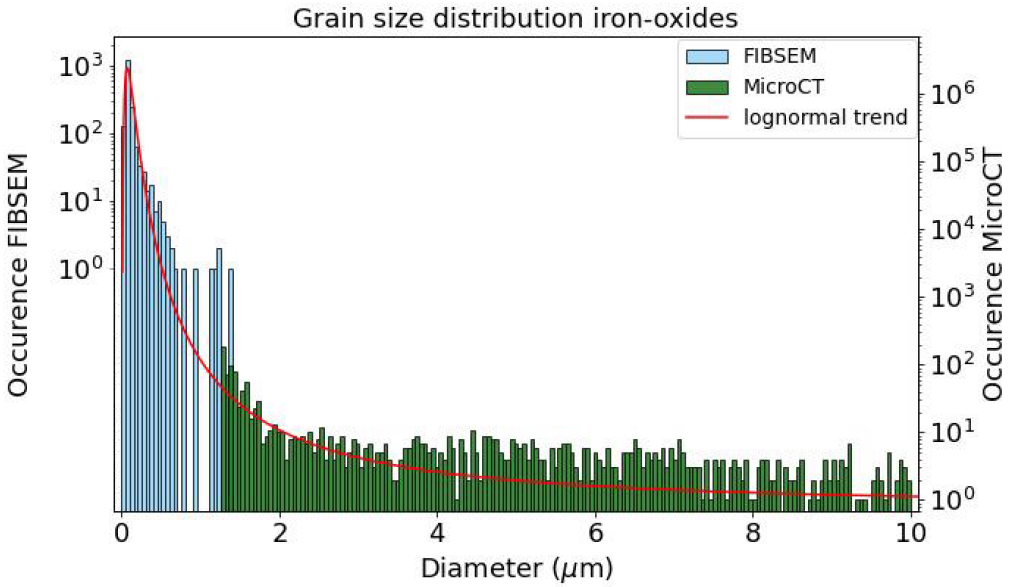

Figure 3. Overview of the non-normalized grain-size distribution. The histograms show the number of iron-oxides obtained from FIB-SEM or MicroCT data. The datasets are scaled to each other using mineral surface area (see main text). The logarithmic trend line shows the fit to these scaled distributions.

with d the diameter of the grain in μm and p the occurrence or probability of finding that grain-size. Note that this probability density function, or pdf, is no longer a lognormal distribution, yet still accurately describes the data (Fig. 3). The function is only valid for grain-sizes between 0 and 10 μm, although it could be extended to larger grain-sizes through rescaling.

To obtain a function from which grain-sizes can be sampled, the probability density function is integrated into a cumulative probability density function (cdf). This function takes a grain-size as input and returns the probability of finding that grain-size or smaller as output. Then to actually create a sampling function, this cdf has to be inverted. By inverting the function, a grain-size could be obtained as function of inputted cumulative probability. However, this inverted function has no analytical expression, so we created a look-up table to be able to sample the function. To create this table we inputted 100,000 diameters between 0 and 10 μm into the cdf, which returned 100,000 cumulative probabilities. Each grain-size–probability pair was then put into the table. To sample grain-sizes from this look-up table we would generate a pool of random numbers, ob-

tained from a uniform distribution between 0 and 1 ($U(0,1)$), equal to the number of samples requested. For each random number we would then extract the corresponding grain-size from the look-up table. Grain-sizes or probabilities not present in the table would be obtained through cubic interpolation of the nearest values. All Python codes to create and sample the grain-size distribution, and the look-up table are available in our repository (Out et al., 2023).

3 Discussion

3.1 Dataset limitations and validation

For this study only one FIB-SEM sample was used from a specific, but typical Hawaiian lava flow. How well this sample represents the sample material of site HW-03, let alone material from other sites, flows, and/or locations is a big unknown. Obtaining data from rock samples using FIB-SEM, however, is not a straightforward task; sample preparation, machine handling, and availability of resources complicate the scanning process. To get the most out of our data, we decided during initial phase of the FIB-SEM analyses to target an area with the highest amount of iron-oxides in view. This implies that relatively many small grains will be present in our FIB-SEM study, leading to an overrepresentation of small grains in our final grain-size distribution.

The overestimation, however, might be somewhat damped through how we constructed the scaling factor. Our scaling factor is dependent on the amount of mineral surface area which probably scales with the number of grains. This might mean that our scaling factor is less sensitive to grain density variations in the studied FIB-SEM area, than, for example, a scaling factor based on volume. In case of volume scaling, the FIB-SEM area would be scaled by a factor of 24,000, independent of the number of grains or amount of mineral surface area present in the studied area. This would most definitively result in a severe overestimation of particles imaged by FIB-SEM compared to particles imaged by MicroCT, because this volume scaling factor is one order of magnitude larger than our scaling factor. We, therefore, consider scaling by grains per mineral interface area a stable protocol to ensure comparability between FIB-SEM and MicroCT results as it dampens local variations of the studied area.

To obtain an independent verification for our method of combining FIB-SEM and MicroCT analyses, we validated our dataset through a scanning electron microscopy (SEM)

image on a sister specimen from site HW03 (de Groot et al., 2013; ter Maat et al., 2018). Two areas of 48.2 × 71.3 μm^2 and 33.2 × 49.0 μm^2 within the sample were imaged with a resolution of 80 and 55 nm per 8-bit pixel respectively. After noise was removed, the images were thresholded at a pixel value of 153 to only retain iron-oxides. Then the major axis m and minor axis n of each grain were determined and grain diameters, d, were calculated using (Yu et al., 2002):

$$d = 2\sqrt{m\frac{n}{\pi}} \tag{2}$$

The diameters of the grains were sorted to produce a normalized histogram with bin-sizes of 0.1 μm ranging between 0.2 and 3.0 μm - straddling the transition from the FIB-SEM realm to the MicroCT range. We discarded grains smaller than 0.2 μm from the SEM data because they would be constructed from two pixels or less. On top of the SEM grain-size data, we overlaid the FIB-SEM and MicroCT normalized data (Fig. 4). The SEM data misses some of the smaller grains, as expected. The trends in the FIB-SEM+MicroCT and SEM datasets for grain-sizes >0.3 μm, however, correspond well. Taking into account that SEM and FIB-SEM are very different scanning techniques compared to MicroCT, we are confident that our constructed grain-size distribution is a proper description of the actual grain-size distribution of iron-oxides in our samples, although it may emphasize small, sub-micron, grains.

3.2 Building models of the physical distribution of iron-oxides

MMT struggles with the smallest particles as they are not detected by MicroCT acquisitions. Although these grains are invisible for MicroCTs, they might still produce a signal in a magnetic surface scan, possibly leading to incorrect magnetic moments of other detected particles (Fabian & De Groot, 2019; Out et al., 2022). However, with the grain-size distribution presented here, it is now possible to study the effect of these ghost grains through generating realistic grain models of basalt and simulating their effect on MMT results in future studies.

To generate a realistic model of the physical distribution of iron-oxide grains in a basaltic sample, we aim to populate a honeycomb structure of the larger minerals obtained from MicroCT analyses with a simulated distribution of small iron-oxides that the MicroCT would miss (Fig. 5). The first step is to extract a honeycomb structure and

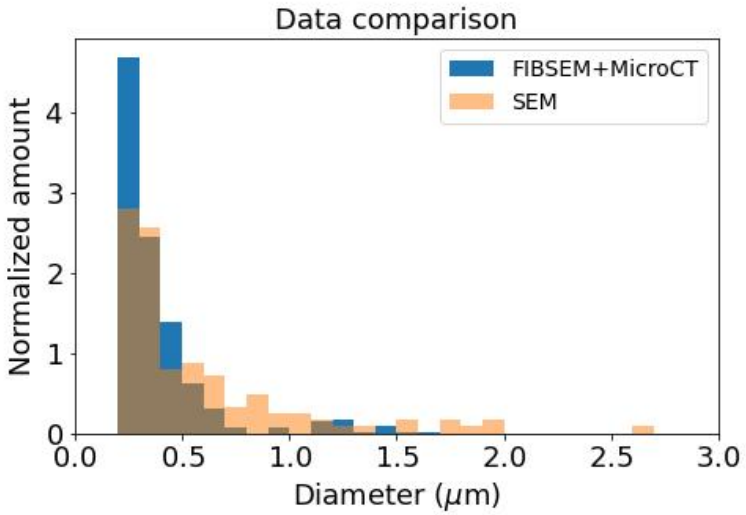

Figure 4. Verification of MicroCT and FIB-SEM data using separate SEM imaged iron-oxides using normalized histograms. Note that the distribution is similar for the two data-series except for the smallest grain-sizes.

the large iron-oxides from a scanned basaltic sample and determine the resolution of the MicroCT. The MicroCT resolution determines how many ghost grains are missing per mm^2 honeycomb structure. By multiplying this ghost grain density (Figure 6) with the honeycomb structure surface area extracted from MicroCT images, we can calculate the total number of missing grains. Then we use the grain-size distribution obtained in this study to make a list of the missing ghost grains and their diameters by feeding the number of missing ghost grains together with the MicroCT resolution into the grain-size distribution sampling function (available in the repository of Out et al., 2023). Finally, we simulate grains from the list of ghost grains and place them on the honeycomb structure obtained from the MicroCT analysis besides the larger iron-oxide particles that were already detected. Hence, by extracting the honeycomb structure and MicroCT resolution, we are able to simulate a realistic distribution of all iron-oxides in a basaltic sample, with diameters down to the superparamagnetic range.

As an example we consider a hypothetical MicroCT analysis with a resolution of 0.1 μm that produced a honeycomb structure with a surface area of 4 mm^2. Then we would need to populate this honeycomb structure with 9×10^5 particles per mm^2 (dashed line in Fig. 6). This implies that we miss 3.6×10^6 ghost grains in the entire sample with

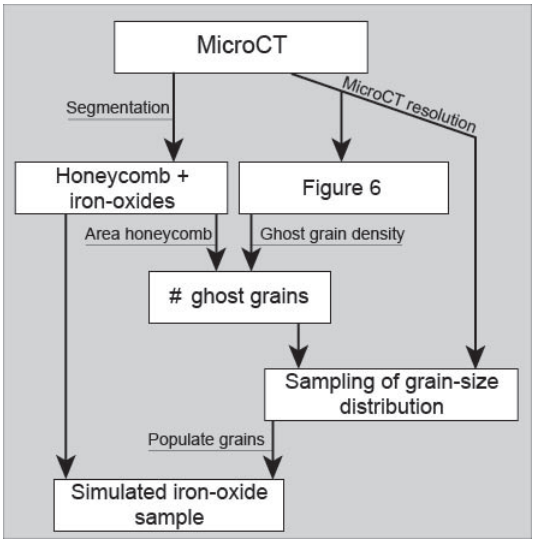

Figure 5. Overview of the protocol to build realistic models of the physical distribution of iron-oxides in a basalt. By segmenting the MicroCT image, we only retain the honeycomb structure and the visible iron-oxides. The MicroCT resolution is required as input for the relation to sample the grain-size distribution of iron-oxides (Fig. 6). Multiplying the ghost grain density with the honeycomb surface area extracted from the MicroCT image, we are able to determine how many grains are left undetected by MicroCT. Given the MicroCT resolution and the number of ghost grains, we sample the grain-size distribution function (see Out et al., 2023) to obtain a list of grain diameters. These grain diameters are used to construct particles that are randomly placed on the extracted honeycomb structure. A graphical overview can be found in the supplementary information (Figure S1).

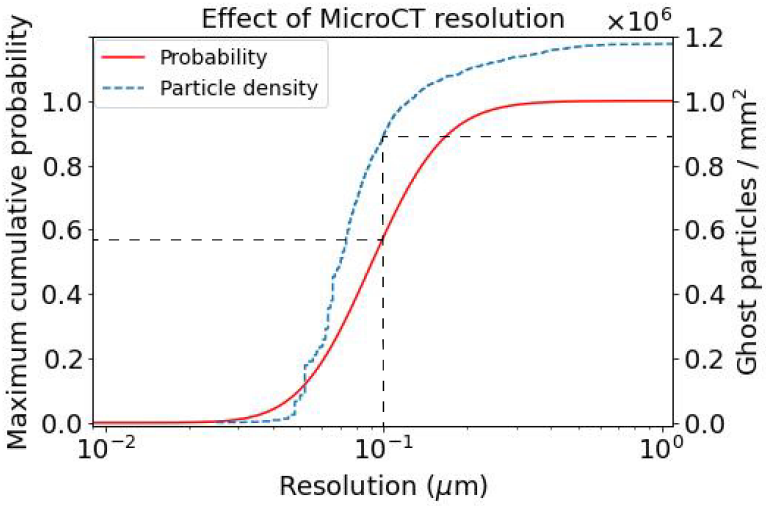

Figure 6. Maximum probability and particles per mm^2 mineral interface area as function of MicroCT resolution. Based on this figure we can determine how many grains have to be sampled from the provided grain-size distribution. By providing the maximum cumulative probability to the grain-size distribution, we can select the maximum grain-size that should be sampled. For example, for 4 mm^2 mineral interface area and a MicroCT resolution of 0.1 μm, we would sample 900.000 particles/mm^2 × 4 mm^2 = 3.6 million particles with a maximum cumulative probability of 0.57. For a resolution larger than 1.0 μm, we would sample 1.20 million grains per mm^2 mineral interface area.

a surface area of 4 mm^2. To obtain the list of grains that we need to add to the honeycomb structure we sample the grain-size distribution 3.6 million times using a maximum cumulative probability of 0.57 (dashed line in Fig. 6) for grains with a diameter between 0 and 0.1 μm. These grains are then randomly placed on the honeycomb structure together next to the larger iron-oxide particles that were already detected with MicroCT.

3.3 Implications for Micromagnetic Tomography

The results of previous MMT based on synthetic samples in which the grain size distribution was controlled (e.g. (most) results in de Groot et al., 2018, 2021)) are most likely not disturbed by ghost grains, because the iron-oxide grains have been sieved for a size larger than the MicroCT resolution. For that reason, their sample mainly consisted of particles larger than 5 μm, which could be easily detected by MicroCT. However, the natural basalt samples used by de Groot et al. (2021) and Kosters et al. (2023) undoubtedly contain undetected ghost grains. Both articles study the magnetic moment of 1,646 iron-oxides detected by MicroCT in a 30 μm thin section of Hawaiian basaltic rock, which is a sister-specimen as subjected to our study. The resolution of the MicroCT used in those studies is $\sim$1 μm and the mineral surface area is $\sim$4 mm^2. According to Fig. 6, this implies the existence of 4.8×10^6 undetected particles, which results in $\sim$3,000 ghost grains per detected iron-oxide.

All of these ghost grains might scramble the signal of the detected iron-oxides leading to erroneous magnetic moments for the detected grains produced by the MMT inversion. Remarkably, both studies do not present unrealistic magnetic moments for the detected iron-oxide particles, and their results are (somewhat) interpretable in terms of magnetic moment and direction. Also, reported trends as function of grain-size and magnetic treatment follow expectations based on earlier work (e.g. Dunlop & Özdemir, 1997). It is therefore likely that, although high in number, the small ghost grains do not have a large enough magnetic moment to have a major contribution to magnetic signal on the surface of the sample. Another possibility is that the spatial resolution of the surface magnetometry data might not be sufficient to locate the weak signal of these ghost particles. As its magnetic moment is highly dependent on the size of a grain (Dunlop & Özdemir, 1997) it is likely that the magnetic moments of larger grains are less affected by ghost grains in an MMT inversion, compared to grains that are just above the detection threshold of the MicroCT analysis used. To characterise the reliability of MMT results as func-

tion of grain size, a future study that models the impact of the undetected ghost grains on MMT results is critical.

4 Conclusions

Here we produced a grain-size distribution of all iron-oxides larger than the superparamagnetic threshold in an Hawaiian basalt by combining MicroCT and FIB-SEM data of sister-specimens. The MicroCT and FIB-SEM datasets could not be combined one-to-one due to volume difference, so they were scaled using the interface area of large, non-iron-oxide, minerals present in the sample (i.e. honeycomb structure), because iron-oxides tend to cluster on the edges of large minerals. Through this scaling procedure we have created a lognormal-like distribution between 20 nm to 10 μm that spans the range of SD, PSD, and MD iron-oxides. This distribution is probably a slight overestimation of the concentration of iron-oxide grains, caused by the choice of FIB-SEM study area with relatively many iron-oxides. This grain-size distribution can be used to populate realistic models of the physical distribution of iron-oxides in a sample; and makes it possible to assess the impact of undetected ghost grains on micromagnetic and MMT studies. Due to the high demands of both MicroCT and FIB-SEM analyses we could only process one sample from a well-characterised Hawaiian lava flow in this study. Future studies can build on our theory of combining FIB-SEM and MicroCT data through the surface area of the honeycomb structure of larger minerals produced by the MicroCT analysis to study other sample material as well.

Data availability statement

The FIB-SEM, MicroCT, and SEM data used for obtaining and verifying, and the jupyter notebooks employed for generating the grain-size distribution and honeycomb structure in this study are available at YODA via https://doi.org/10.24416/UU01-QNASXB with a CC-BY-NC-4.0 license (Out et al., 2023). Numerical calculations were executed with support of NumPy (Harris et al., 2020), SciPy (Virtanen et al., 2020), OpenCV (Bradski, 2000), and Matplotlib (Hunter, 2007) Python libraries. The MicroCT analysis for this study was generated using Dragonfly software, Version 2022.1.0.1259 for Windows. Object Research Systems (ORS) Inc, Montreal, Canada, 2022.

Acknowledgments

This project has received funding from the European Research Council (ERC) under the European Union's Horizon 2020 research and innovation program (Grant agreement No. 851460 to L.V. de Groot). This publication results from work carried out under transnational access action under the support of EXCITE – EC- HORIZON 2020 – INFRAIA 2020 Integrating Activities for Starting Communities (Grant agreement No. 101005611).

References

Berndt, T., Muxworthy, A. R., & Fabian, K. (2016). Does size matter? statistical limits of paleomagnetic field reconstruction from small rock specimens. *Journal of Geophysical Research: Solid Earth*, *121*(1), 15–26.

Bradski, G. (2000). The OpenCV Library. *Dr. Dobb's Journal of Software Tools*.

de Groot, L. V., Biggin, A. J., Dekkers, M. J., Langereis, C. G., & Herrero-Bervera, E. (2013, 12). Rapid regional perturbations to the recent global geomagnetic decay revealed by a new Hawaiian record. *Nature Communications*, *4*(1), 2727. Retrieved from `www.nature.com/naturecommunicationshttp://www.nature.com/articles/ncomms3727` doi: 10.1038/ncomms3727

De Groot, L. V., Fabian, K., Bakelaar, I. A., & Dekkers, M. J. (2014). Magnetic force microscopy reveals meta-stable magnetic domain states that prevent reliable absolute palaeointensity experiments. *Nature Communications*, *5*(1), 4548.

de Groot, L. V., Fabian, K., Béguin, A., Kosters, M. E., Cortés-Ortuño, D., Fu, R. R., ... Barnhoorn, A. (2021). Micromagnetic tomography for paleomagnetism and rock-magnetism. *Journal of Geophysical Research: Solid Earth*, *126*(10), e2021JB022364.

de Groot, L. V., Fabian, K., Béguin, A., Reith, P., Barnhoorn, A., & Hilgenkamp, H. (2018). Determining individual particle magnetizations in assemblages of micrograins. *Geophysical Research Letters*, *45*(7), 2995–3000.

Dunlop, D. J., & Özdemir, Ö. (1997). *Rock Magnetism*. Cambridge University Press. Retrieved from `https://www.cambridge.org/core/product/identifier/9780511612794/type/book` doi: 10.1017/cbo9780511612794

Einsle, J. F., Harrison, R. J., Kasama, T., Conbhuí, P. Ó., Fabian, K., Williams, W., ... Midgley, P. A. (2016). Multi-scale three-dimensional charac-

terization of iron particles in dusty olivine: Implications for paleomagnetism of chondritic meteorites. *American Mineralogist*, *101*(9), 2070–2084. Retrieved from https://doi.org/10.2138/am-2016-5738CCBY doi: doi:10.2138/am-2016-5738CCBY

Fabian, K., & De Groot, L. V. (2019, 2). A uniqueness theorem for tomography-assisted potential-field inversion. *Geophysical Journal International*, *216*(2), 760–766. Retrieved from http://arxiv.org/abs/1712.06136https://academic.oup.com/gji/article/216/2/760/5151336 doi: 10.1093/gji/ggy455

Glenn, D. R., Fu, R. R., Kehayias, P., Le Sage, D., Lima, E. A., Weiss, B. P., & Walsworth, R. L. (2017, 8). Micrometer-scale magnetic imaging of geological samples using a quantum diamond microscope. *Geochemistry, Geophysics, Geosystems*, *18*(8), 3254–3267. Retrieved from https://onlinelibrary.wiley.com/doi/abs/10.1002/2017GC006946 doi: 10.1002/2017GC006946

Harris, C. R., Millman, K. J., van der Walt, S. J., Gommers, R., Virtanen, P., Cournapeau, D., ... Oliphant, T. E. (2020, 9). Array programming with NumPy. *Nature*, *585*(7825), 357–362. Retrieved from http://www.nature.com/articles/s41586-020-2649-2 doi: 10.1038/s41586-020-2649-2

Hunter, J. D. (2007, 5). Matplotlib: A 2D Graphics Environment. *Computing in Science & Engineering*, *9*(3), 90–95. Retrieved from http://nipy.scipy.http://ieeexplore.ieee.org/document/4160265/ doi: 10.1109/MCSE.2007.55

Kosters, M. E., de Boer, R. A., Out, F., Cortés-Ortuño, D. I., & de Groot, L. V. (2023). Unraveling the magnetic signal of individual grains in a hawaiian lava using micromagnetic tomography. *Geochemistry, Geophysics, Geosystems*, *24*(4), e2022GC010462. Retrieved from https://agupubs.onlinelibrary.wiley.com/doi/abs/10.1029/2022GC010462 (e2022GC010462 2022GC010462) doi: https://doi.org/10.1029/2022GC010462

Lindblad, J. (2005). Surface area estimation of digitized 3d objects using weighted local configurations. *Image and Vision Computing*, *23*(2), 111–122.

Nagy, L., Williams, W., Muxworthy, A. R., Fabian, K., Almeida, T. P., Conbhui, P. O., & Shcherbakov, V. P. (2017). Stability of equidimensional pseudo-single-domain magnetite over billion-year timescales. *Proceedings of the National*

Academy of Sciences of the United States of America, *114*(39), 10356-10360. doi: 10.1073/pnas.1708344114

Néel, L. (1955, 4). Some theoretical aspects of rock-magnetism. *Advances in Physics*, *4*(14), 191–243. Retrieved from https://www.tandfonline.com/doi/abs/10.1080/00018735500101204http://www.tandfonline.com/doi/abs/10.1080/00018735500101204 doi: 10.1080/00018735500101204

Nikolaisen, E. S., Harrison, R. J., Fabian, K., & McEnroe, S. A. (2020). Hysteresis of natural magnetite ensembles: Micromagnetics of silicate-hosted magnetite inclusions based on focused-ion-beam nanotomography. *Geochemistry, Geophysics, Geosystems*, *21*(11), e2020GC009389.

Out, F., Cortés-Ortuñno, D., Fabian, K., van Leeuwen, T., & de Groot, L. V. (2022). A first-order statistical exploration of the mathematical limits of micromagnetic tomography. *Geochemistry, Geophysics, Geosystems*. doi: e2021GC010184

Out, F., de Boer, R. A., Walmsley, J., & de Groot, L. V. (2023). *Replication Data for: Modeling the Distribution of Iron-oxides in Basalt by combining FIB-SEM and MicroCT Measurements.* YODA. Retrieved from https://public.yoda.uu.nl/geo/UU01/QNASXB.html doi: 10.24416/UU01-QNASXB

Smirnov, A. (2006). Memory of the magnetic field applied during cooling in the low-temperature phase of magnetite: Grain size dependence. *Journal of Geophysical Research: Solid Earth*, *111*(B12).

Tauxe, L. (2010). *Essentials of paleomagnetism.* Univ of California Press.

Tauxe, L., & Yamazaki, T. (2015). Paleointensities. In *Treatise on geophysics* (pp. 461–509). Elsevier. doi: 10.1016/B978-0-444-53802-4.00107-X

ter Maat, G. W., Pennock, G. M., & de Groot, L. V. (2018). Data descriptor: A chemical, crystallographic and magnetic characterisation of individual iron-oxide grains in Hawaiian lavas. *Scientific Data*, *5*, 1–9. doi: 10.1038/sdata.2018.162

Virtanen, P., Gommers, R., Oliphant, T. E., Haberland, M., Reddy, T., Cournapeau, D., ... van Mulbregt, P. (2020, 3). SciPy 1.0: fundamental algorithms for scientific computing in Python. *Nature Methods*, *17*(3), 261–272. Retrieved from https://doi.org/10.1038/s41592-019-0686-2http://www.nature.com/articles/s41592-019-0686-2 doi: 10.1038/s41592-019-0686-2

512 Yu, Y., Dunlop, D. J., & Özdemir, Ö. (2002). Partial anhysteretic remanent mag-
513 netization in magnetite 1. additivity. *Journal of Geophysical Research: Solid*
514 *Earth*, *107*(B10), EPM–7.

Modeling the Distribution of Iron-oxides in Basalt by combining FIB-SEM and MicroCT Measurements

Frenk Out[1], Rosa A. de Boer[1], John Walmsley[2], Lennart V. de Groot[1]

[1]Paleomagnetic laboratory Fort Hoofddijk, Department of Earth Sciences, Utrecht University, Budapestlaan 17, 3584 CD Utrecht, The Netherlands.

[2]Department of Materials Science & Metallurgy, University of Cambridge, 27 Charles Babbage Road, CB3 0FS Cambridge, United Kingdom.

Key Points:

- We produced a grain-size distribution of iron-oxides in a typical Hawaiian basalt from the superparamagnetic threshold (∼40 nm) to 10 micron
- We combined FIB-SEM and MicroCT data from sister specimens by normalizing them to the mineral surface area of the non-magnetic minerals
- Our grain-size distribution can be used to populate realistic models of iron-oxides in a Hawaiian basalt

Corresponding author: Frenk Out, `f.out@uu.nl`

Abstract

Micromagnetic tomography (MMT) aims to go beyond paleomagnetic measurements on bulk samples by obtaining magnetic moments for individual iron-oxide grains present in a sample. To obtain accurate MMT results all magnetic sources and all their magnetic signals should be known. Small particles (<<1 μm) are often not detected by MicroCT analyses, but do have a magnetic signal, and therefore hamper obtaining reliable MMT results. Currently it is unknown how many of these small 'ghost grains' are present in basaltic samples. Here we aim to obtain a realistic grain-size distribution for iron-oxides in a typical Hawaiian basalt. We characterize the entire grain-size range of interest to paleomagnetism, from the superparamagnetic threshold of ∼40 nm to multidomain grains with sizes up to 10 μm. This requires a combination of FIB-SEM slice-and-view and MicroCT techniques: FIB-SEM characterizes the grains between 20 nm and 1 μm and MicroCT detects iron-oxides >750 nm. The FIB-SEM and MicroCT data are combined through normalizing the grain-size distribution using the surface area of non-magnetic minerals that are characterised in both datasets. Then, a lognormal-like grain-size distribution is acquired for the entire grain-size range. Our dataset enables future studies to populate (MMT) models with a realistic distribution of even the smallest iron-oxide grains, which ultimately may shed light on the confounding influence of such ghost grains on MMT results.

Plain Language Summary

Micromagnetic tomography (MMT) is a promising new technique that extracts high-quality magnetic information from lavas. Magnetic particles in lavas obtain a magnetic signal while cooling in presence of Earth's magnetic field. However, not all particles store the signal well, meaning that both good and bad recorders are present. Classical paleomagnetic techniques measure the magnetic signal of all recorders together, i.e. the bulk signal. MMT, however, acquires the signal from individual recorders in the lava, enabling selecting only the good recorders and rejecting the signal of bad recorders. MMT needs two pieces of information: (1) the surface magnetic field produced by recorders and (2) the location of all recorders in the lava. Unfortunately, the position of recorders smaller than ∼1 μm are often unknown due to measurement limitations. If these small particles are not detected, they may scramble the calculated signal of larger recorders. To investigate how many disruptive undetected grains are present, we scanned a small vol-

ume of lava on high resolution to extract all magnetic recorders and obtain a grain-size distribution. With this distribution we may estimate if these small recorders distort the signal of larger detected grains.

1 Introduction

Volcanic rocks are often perceived to be excellent recorders of paleomagnetic fields, although only a small portion of all minerals in a volcanic rock has magnetic properties. These minerals, iron-oxide grains, present in a lava acquire a magnetization by cooling in the Earth's magnetic field. Their magnetization is thus a thermo-remanent magnetization (TRM), and these magnetic signals are regarded to be stable, often over millions or billions of years (e.g. Dunlop & Özdemir, 1997; Tauxe & Yamazaki, 2015).

Small particles, or single domain (SD) grains, have two configurations for storing their magnetic signal: either parallel or anti-parallel to the grain's easy axis. One of these two options is selected at random but with a slight preference to align with the prevailing magnetic field (e.g. Tauxe, 2010; Berndt et al., 2016). In slightly larger particles, which are often referred to as pseudo-single domain (PSD) grains, the magnetic signal is stored in a more complex vortex structure. Fortunately, this signal usually represents the original imparting magnetic field accurately (Nagy et al., 2017). The last group of particles are iron-oxides with diameters >1 μm and belong to the multi-domain (MD) class. Although these MD grains may store magnetic signals for millions of years, their expression of the past field is often disturbed, overprinted, unstable, or lost (e.g. De Groot et al., 2014). This instability is caused by magnetic reassembling of the original magnetic structure of a grain over time to achieve energy minimization (Néel, 1955). MD grains are therefore mostly perceived as bad paleomagnetic recorders, while SD and PSD grains are considered to be more reliable recorders of paleomagnetic fields. To make it even more difficult, most natural rock samples consist of a mixture of SD, PSD and MD grains. The combination of these good and bad recorders in rocks is the main reason that generally only 10 to 20% of all paleointensity experiments pass sufficient selection criteria to yield usable results (e.g. Tauxe & Yamazaki, 2015; Nagy et al., 2017).

To circumvent the problem of acquiring signals simultaneously from good and bad recorders, de Groot et al. (2018) proposed a new paleomagnetic technique to obtain magnetic moments of individual iron-oxide grains in a sample: micromagnetic tomography (MMT). MMT infers magnetic moments by first acquiring a magnetic surface image of a (cut-out of a) thin-section of a sample using a surface magnetometry technique (e.g. a Quantum Diamond Microscope: Glenn et al., 2017). Then, the position of each iron-oxide grain in that sample is obtained with X-Ray micro computed tomography (MicroCT).

These two pieces of information are combined in a mathematical inversion to retrieve individual magnetic moments by minimizing residuals in the magnetic surface map. Both de Groot et al. (2021) and Kosters et al. (2023) have shown the capabilities of MMT on Hawaiian rock samples. The mathematical uncertainties of the technique have been modeled in Out et al. (2022).

Theoretically, MMT is able to retrieve the magnetic moment of even the smallest SD iron-oxide particles. These particles are unfortunately often not detected by present-day MicroCT equipment, because these machines have resolutions down to 350-500 nm. As a grain can only be reliably resolved if it consists of a couple of voxels, it is only possible to detect particles with a diameter of >1 μm. Consequently, SD and PSD particles may produce a detectable magnetic signal in the magnetic surface scan, while they do not show up in the MicroCT data. This problem challenges MMT, because the method can only deliver unique and reliable results if all measured magnetic signals originate from detected iron-oxides in the sample (Fabian & De Groot, 2019). Currently it is unknown how many small iron-oxides that go undetected by the MicroCT analyses (i.e. ghost particles) are present in (Hawaiian) basaltic lavas. Here we aim to image and characterize the distribution of these ghost particles using Focused Ion Beam Scanning Electron Microscopy (FIB-SEM), following the slice-and-view approach of Nikolaisen et al. (2020). With FIB-SEM it is possible to image a sample of micrometer size with a resolution of $\sim$20 nm by slicing (or milling) through the sample and imaging the cleared surface. In this way, a 3D reconstruction of the sample volume with these previous undetected iron-oxide particles can be reconstructed. Since iron-oxide grains reflect electrons well, the particles are simply detected through backscattered electron images obtained with scanning electron microscopy. Nikolaisen et al. (2020) used the grain shapes to model micromagnetic properties of the individual grains that were characterized by the FIB-SEM analyses. Here we will use the three dimensional characterisation of the small iron-oxides present in our sample to reconstruct a grain-size distribution. We combine the grain-size distribution obtained using the FIB-SEM with the MicroCT analyses on the same sample material to obtain a grain-size distribution spanning both the nanometer and micrometer scale. Linking these two datasets, however, is not straightforward because iron-oxides are not uniformly present in a rock sample but cluster around large mineral interfaces. We therefore use the surface area of relatively large, non-magnetic, grains in both the FIB-SEM and MicroCT data to normalize and combine the grain-size distributions ob-

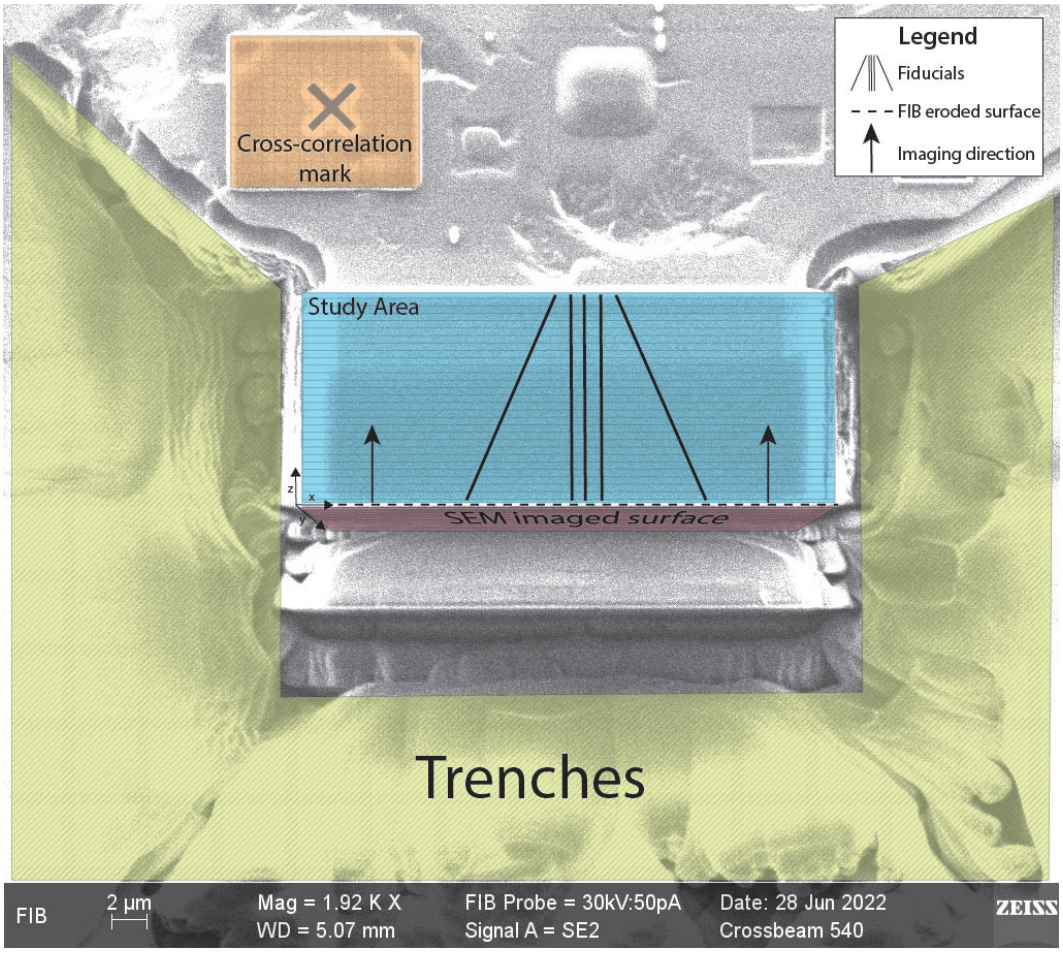

Figure 1. Overview of the study area within a Hawaiian basalt examined by slice-and-view through FIB-SEM. After the ion beam removed a 20.18 nm slice from the bottom of the study area, a backscattered and secondary reflected electron image is recorded. Instrumental drift is constrained by calibrating the FIB-SEM every 100 slices using the cross-correlation mark in the top left corner.

tained from both analyses. Lastly, we will demonstrate how these particles can be placed in numerical models to simulate a realistic basalt sample. With these models, it might ultimately be possible to investigate the effect of resolution limitations of MicroCT leading to the presence of ghost particles in MMT analyses.

2 Grain-size distribution

Pivotal in obtaining a realistic grain-size distribution is acquiring dimensional properties of all iron-oxide grains present in basaltic rocks. The sample we have used in this

study was taken from the 1907 lava flow from Hawaii (HW-03; de Groot et al., 2013; ter Maat et al., 2018)). The MicroCT data of this sample had already been studied by de Groot et al. (2021) and Kosters et al. (2023), facilitating the detection of grains larger than ∼1 μm, but leaving most of the SD and PSD particles undetected. Fortunately, with the help of FIB-SEM (e.g. Einsle et al., 2016; Nikolaisen et al., 2020) these remaining SD and PSD grains could finally be made visible. FIB-SEM allows a pixel size of 10 nm and a field of view close to 20 by 20 μm, which enables the detection of both the smallest SD grains above the superparamagnetic threshold of 40 nm (Dunlop & Özdemir, 1997) and large MD grains of >1 μm, which are normally at the lower detection limit of MicroCT.

2.1 Image acquisition with FIB-SEM

We applied FIB-SEM on a sample of HW-03, following the slice-and-view procedure described in Einsle et al. (2016) and Nikolaisen et al. (2020). A 60 μm thick slice with a diameter of 2 mm was extracted from the specimen and coated with a nanometer thick layer of gold. Around the edges of the sample, silver was applied with a toothpick so that electrons could easily pass through the sample. The sample was placed in a Zeiss Crossbeam 540 after which we searched the top of the sample for a 20 x 20 μm area containing many small iron-oxides. This area was prepared for the slice-and-view procedure by first applying a 1 μm thick layer of platinum while maintaining an ion beam current of 700 pA and an accelerating voltage of 30 kV. This accelerating voltage did not change unless explicitly stated otherwise.

Then, five 0.5 µm deep fiducials were engraved with a current of 50 pA (Fig. 1). The three central fiducials were created parallel to each other to enable image alignment during data processing. The outer two fiducials were created under an angle of 25 degrees with respect to the three central fiducials. These two fiducials ensured that the real thickness of the individual image slices could later be checked. To make these fiducials visible, a 0.6 μm thick carbon layer was deposited on top of the platinum layer with an ion beam current of 700 pA and a dwell-time of 400 seconds. Then, three trenches with a depth of 25 μm and an area of 27 by 46 μm^2 were eroded at three sides of the selected area. For this erosion procedure, we used an ion beam current kept at 15 nA with a back-and-forth milling pattern (bidirectional). Using the same bidirectional routine, the current was reduced from 15 nA to 7 nA to create smooth trenches next to the studied area.

Instrumental drift during measurements was reduced to a minimum by applying a cross-correlation mark outside the studied area (Fig. 1).

The data acquisition process was initiated after a 20.18 nm slice of the sample area was removed with FIB (beam current at 1.5 nA with an accelerating voltage between 1 to 6 kV). Backscattered and secondary reflected electrons images where obtained using SEM, after which a 20.18 nm layer of sample was removed using FIB. After this procedure was repeated a hundred times instrumental drift was corrected by checking alignment with the cross-correlation mark. The entire process was finished in one day, in which 601 grayscale images of both backscattered and secondary reflected electrons were saved in TIFF format. Each file encompassed a pixel area of 3072 x 2104 pixels with a pixel size of 10.09 nm and a 8-bit grayscale. The total volume of sample analysed was therefore 31.0 x 21.2 x 12.1 μm^3.

2.2 Dataprocessing

2.2.1 Extracting particles from FIB-SEM data

After image acquisition, a grain-size distribution could be extracted from the data. Every data processing step was executed with Python 3 and the OpenCV library (Bradski, 2000). We initiated our data processing by loading the 601 backscattered electron images and aligning them using the three parallel fiducials and the matchTemplate function of OpenCV. After alignment, we removed all duplicate images. To remove the effects of both curtaining and the platina and carbon deposited layers, every image was cropped to 2600 $\times$ 1000 pixels.

Through denoising and thresholding, SD and PSD iron-oxides could be extracted from FIB-SEM images as shown by Nikolaisen et al. (2020). However, we designed the extraction process in such a way that both the surface and the centre of each iron-oxide grain were properly retrieved. We initiated denoising by 2$\times$2 binning of the 549 remaining images, which resulted into 1300 $\times$ 500 pixels per image. A non-local means denoising filter from OpenCV (`fastNlMeansDenoisingMulti`) was used with a search windowsize of 20 pixels, a filter strength of 20, and template windowsize of 3 pixels applied in the x, y, and z-direction. Each image was then thresholded at a pixelvalue of 220. After thresholding, all images are stacked together into one 3D-volume. In this 3D-volume,

we grouped connected pixels into grains. With this high threshold, we have only obtained the brightest central iron-oxide pixels.

However, the iron-oxide grains are not properly imaged yet, because the sides of the grains frequently have a lower pixel value than their center and thus have dropped out in the previous thresholding step. To correctly image the boundary of the iron-oxides we applied a lower threshold value of 160 instead of 220 to the previous set of images. Then we applied the canny edge algorithm of OpenCV (`Canny`). This algorithm detects spatial changes in pixel value and draws, based on that change, boundaries between pixel values. After drawing boundaries, small gaps in the boundaries were closed using the morphology close operation in order to create enclosed areas. Again, all images were combined into a 3D-volume and connected pixels were grouped into grains. However, the low threshold outputted both well defined grain shapes of iron-oxides and poorly defined shapes of other unwanted minerals. To get rid of these unwanted minerals, we mapped the grains obtained with high thresholding (poorly defined boundaries, most certainly iron-oxides) on top of the grains obtained with low thresholding (well defined boundaries, possible iron-oxides) to only remain with actual iron-oxides. Lastly, we removed all iron-oxides that extend beyond the edges of the FIB-SEM domain. We calculated the volume of 1,558 remaining iron-oxides, and transformed these volumes into an equivalent diameter assuming spherical grains.

2.2.2 Scaling FIB-SEM and MicroCT data

To obtain a grain-size distribution spanning the entire range of naturally occurring iron-oxides, we combined our FIB-SEM data with MicroCT data that was obtained on a sister specimen of HW-03 by Kosters et al. (2023). Since iron-oxides are not homogeneously distributed throughout the rock, it is not straightforward to link MicroCT data one-to-one to FIB-SEM data based on volume. Most iron-oxides are positioned on the interface between larger grains (mainly plagioclase and pyroxene); especially the smallest iron-oxides attach themselves to this 'honeycomb' structure of other minerals (Fig. 2). Because this honeycomb structure of relatively large minerals can be imaged properly using MicroCT, it allows for extrapolating the number of undetected small iron-oxides from the FIB-SEM analysis to the MicroCT data and hence produce a continuous grain-size distribution over both analyses.

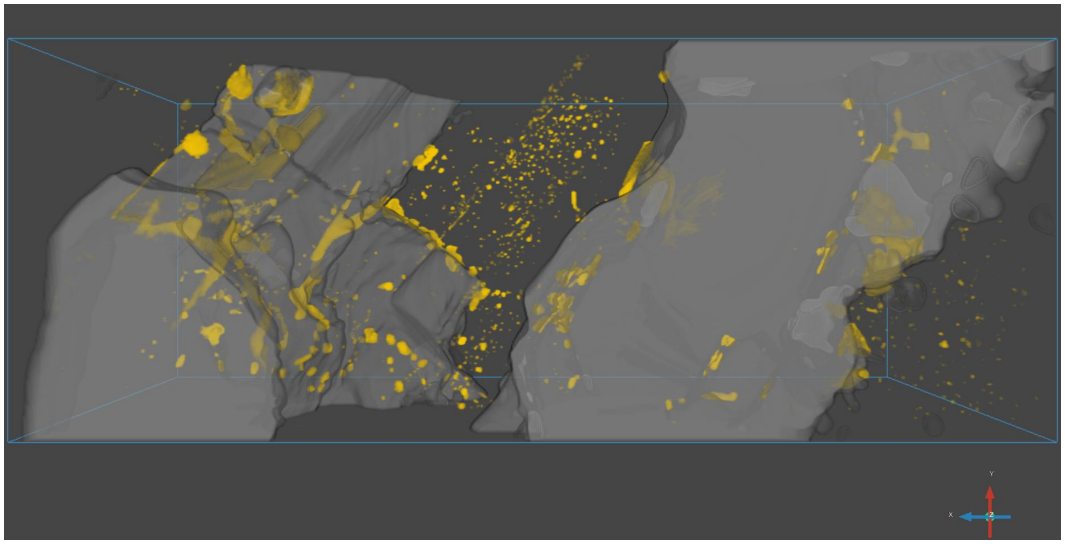

Figure 2. Overview of the 26.2 × 10.1 × 10.5 μm^3 volume exposed to the slice-and-view procedure with FIB-SEM. The large grains are indicated by a grayish color. The iron-oxides residing in this volume are indicated in yellow-brown. Note that most iron-oxides reside on the large mineral interfaces.

Characterizing the mineral surface area of the larger minerals, mainly plagioclase and pyroxene, required reprocessing the FIB-SEM data, with this specific goal in mind. First, the FIB-SEM dataset was denoised using a non-local means filter; then we applied a median filter with a spherical footprint of 13 pixels in diameter to smooth out irregularities at the boundaries. After this pre-processing we applied a K-means algorithm to create five groups of pixels. For each individual image, we removed the first group because it corresponded to drilling artifacts. Additionally, we removed all areas smaller than 3000 pixels, because these areas do not represent grain interfaces of the larger minerals present in the sample that are typically occupied by iron-oxides. Finally, the mineral surface area was calculated for the remaining pixel values using a 'Lindblad' algorithm (Lindblad, 2005). The mineral surface area consisted of about 3.8 × 10^6 squared pixels that correspond to an area of 1.53 × 10^{-3} mm^2. Fig. 2 shows the position of the mineral surface area together with the iron-oxides.

To calculate the mineral surface area in the MicroCT dataset, we started with raw MicroCT data and processed it using Dragonfly software. After loading the DICOM files, we cropped about 100 μm on both sides of the sample to remove scanning residuals. To align the sample with the coordinate axes, we rotated the sample 0.85° clockwise around

the z-axis, 0.50° anticlockwise around the x-axis, and resampled the image with 0.75 μm pixel size. Then the image was cropped further, which resulted into a region of 1979 × 44 × 1901 voxels. We denoised the image by applying a non-local means filter with a 3D spherical kernel size of 11 pixels. To create a larger contrast we applied a median filter with a 3D spherical kernel size of 13 pixels. The different minerals were separated by applying a K-means filter of 3 groups, of which the group with the highest pixel value corresponds to iron-oxides. The other two groups chiefly consisted of plagioclase and pyroxene. Since we observed that SD and PSD iron-oxides tend to cluster on the interfaces of these minerals, we applied a 'sobel edge detection' filter to these groups. The result of this filter enabled us to create a honeycomb structure of the sample, on which we could populate SD and PSD iron-oxides to create realistic models of basalts. This mineral surface area of 4.00 mm^2 is approximately 2,620 times larger than the surface area found in the FIB-SEM dataset. This means that we need to multiply the number of FIB-SEM grains by 2,620 to scale correctly to the MicroCT dataset. This resulted into a combined dataset of 4.7 $\times 10^6$ FIB-SEM and 1.6 $\times 10^3$ MicroCT iron-oxide grains. The FIB-SEM and MicroCT datasets can now be combined to produce a continuous grain-size distribution of iron-oxides for the entire range of interest (Fig. 3). The median grain-size has a diameter of 70 nm. From 30 to 70 nm the occurrence rapidly increases, after which the occurrence of grain diameters between 70 nm and 10 μm follows are more gradually decaying trend.

2.3 Constructing the grain-size distribution

The trend in grain-size distribution can be described using a lognormal-like distribution between 20 nm and 10 μm. We have chosen the lognormal distribution, because this distribution is frequently used to describe grain-sizes for e.g. magnetite powders (Smirnov, 2006; Yu et al., 2002). Nevertheless, the lognormal trend line was originally fitted to the 10^{th}-logarithm of the data. This logarithm ensures a better fit to grain-sizes larger than 70 nm. Through an iterative procedure reducing the least-squares error of our fit to the data, we found the best fitting distribution after which we transformed it back to linear space:

$$p = 3.51 * 10^{-6+\frac{5.61}{d\sqrt{2\pi}}e^{-\frac{\ln^2(0.60d)}{6.29}}} \text{ if } d : [0, 10] \quad (1)$$

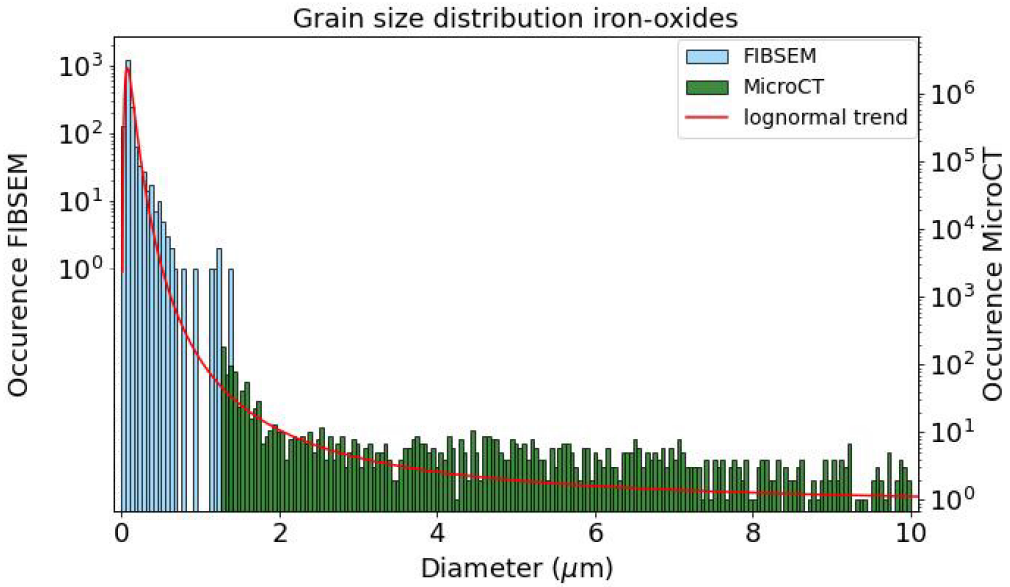

Figure 3. Overview of the non-normalized grain-size distribution. The histograms show the number of iron-oxides obtained from FIB-SEM or MicroCT data. The datasets are scaled to each other using mineral surface area (see main text). The logarithmic trend line shows the fit to these scaled distributions.

with d the diameter of the grain in μm and p the occurrence or probability of finding that grain-size. Note that this probability density function, or pdf, is no longer a lognormal distribution, yet still accurately describes the data (Fig. 3). The function is only valid for grain-sizes between 0 and 10 μm, although it could be extended to larger grain-sizes through rescaling.

To obtain a function from which grain-sizes can be sampled, the probability density function is integrated into a cumulative probability density function (cdf). This function takes a grain-size as input and returns the probability of finding that grain-size or smaller as output. Then to actually create a sampling function, this cdf has to be inverted. By inverting the function, a grain-size could be obtained as function of inputted cumulative probability. However, this inverted function has no analytical expression, so we created a look-up table to be able to sample the function. To create this table we inputted 100,000 diameters between 0 and 10 μm into the cdf, which returned 100,000 cumulative probabilities. Each grain-size–probability pair was then put into the table. To sample grain-sizes from this look-up table we would generate a pool of random numbers, ob-

tained from a uniform distribution between 0 and 1 ($U(0,1)$), equal to the number of samples requested. For each random number we would then extract the corresponding grain-size from the look-up table. Grain-sizes or probabilities not present in the table would be obtained through cubic interpolation of the nearest values. All Python codes to create and sample the grain-size distribution, and the look-up table are available in our repository (Out et al., 2023).

3 Discussion

3.1 Dataset limitations and validation

For this study only one FIB-SEM sample was used from a specific, but typical Hawaiian lava flow. How well this sample represents the sample material of site HW-03, let alone material from other sites, flows, and/or locations is a big unknown. Obtaining data from rock samples using FIB-SEM, however, is not a straightforward task; sample preparation, machine handling, and availability of resources complicate the scanning process. To get the most out of our data, we decided during initial phase of the FIB-SEM analyses to target an area with the highest amount of iron-oxides in view. This implies that relatively many small grains will be present in our FIB-SEM study, leading to an overrepresentation of small grains in our final grain-size distribution.

The overestimation, however, might be somewhat damped through how we constructed the scaling factor. Our scaling factor is dependent on the amount of mineral surface area which probably scales with the number of grains. This might mean that our scaling factor is less sensitive to grain density variations in the studied FIB-SEM area, than, for example, a scaling factor based on volume. In case of volume scaling, the FIB-SEM area would be scaled by a factor of 24,000, independent of the number of grains or amount of mineral surface area present in the studied area. This would most definitively result in a severe overestimation of particles imaged by FIB-SEM compared to particles imaged by MicroCT, because this volume scaling factor is one order of magnitude larger than our scaling factor. We, therefore, consider scaling by grains per mineral interface area a stable protocol to ensure comparability between FIB-SEM and MicroCT results as it dampens local variations of the studied area.

To obtain an independent verification for our method of combining FIB-SEM and MicroCT analyses, we validated our dataset through a scanning electron microscopy (SEM)

image on a sister specimen from site HW03 (de Groot et al., 2013; ter Maat et al., 2018). Two areas of 48.2 × 71.3 μm^2 and 33.2 × 49.0 μm^2 within the sample were imaged with a resolution of 80 and 55 nm per 8-bit pixel respectively. After noise was removed, the images were thresholded at a pixel value of 153 to only retain iron-oxides. Then the major axis m and minor axis n of each grain were determined and grain diameters, d, were calculated using (Yu et al., 2002):

$$d = 2\sqrt{m\frac{n}{\pi}} \tag{2}$$

The diameters of the grains were sorted to produce a normalized histogram with bin-sizes of 0.1 μm ranging between 0.2 and 3.0 μm - straddling the transition from the FIB-SEM realm to the MicroCT range. We discarded grains smaller than 0.2 μm from the SEM data because they would be constructed from two pixels or less. On top of the SEM grain-size data, we overlaid the FIB-SEM and MicroCT normalized data (Fig. 4). The SEM data misses some of the smaller grains, as expected. The trends in the FIB-SEM+MicroCT and SEM datasets for grain-sizes >0.3 μm, however, correspond well. Taking into account that SEM and FIB-SEM are very different scanning techniques compared to MicroCT, we are confident that our constructed grain-size distribution is a proper description of the actual grain-size distribution of iron-oxides in our samples, although it may emphasize small, sub-micron, grains.

3.2 Building models of the physical distribution of iron-oxides

MMT struggles with the smallest particles as they are not detected by MicroCT acquisitions. Although these grains are invisible for MicroCTs, they might still produce a signal in a magnetic surface scan, possibly leading to incorrect magnetic moments of other detected particles (Fabian & De Groot, 2019; Out et al., 2022). However, with the grain-size distribution presented here, it is now possible to study the effect of these ghost grains through generating realistic grain models of basalt and simulating their effect on MMT results in future studies.

To generate a realistic model of the physical distribution of iron-oxide grains in a basaltic sample, we aim to populate a honeycomb structure of the larger minerals obtained from MicroCT analyses with a simulated distribution of small iron-oxides that the MicroCT would miss (Fig. 5). The first step is to extract a honeycomb structure and

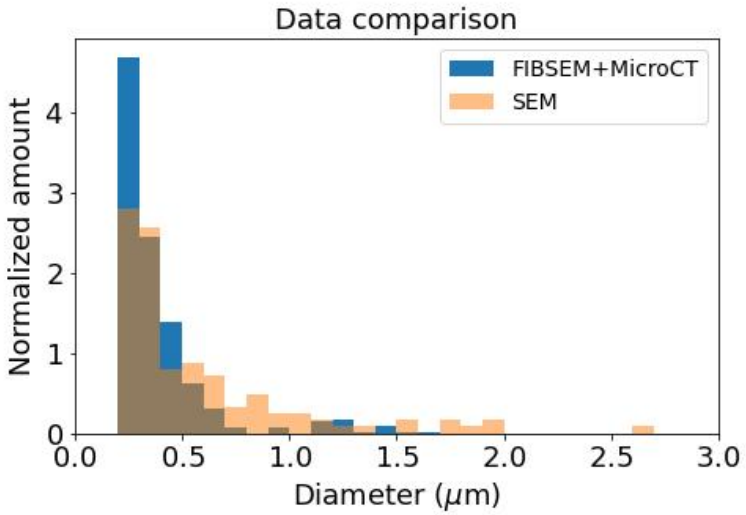

Figure 4. Verification of MicroCT and FIB-SEM data using separate SEM imaged iron-oxides using normalized histograms. Note that the distribution is similar for the two data-series except for the smallest grain-sizes.

the large iron-oxides from a scanned basaltic sample and determine the resolution of the MicroCT. The MicroCT resolution determines how many ghost grains are missing per mm^2 honeycomb structure. By multiplying this ghost grain density (Figure 6) with the honeycomb structure surface area extracted from MicroCT images, we can calculate the total number of missing grains. Then we use the grain-size distribution obtained in this study to make a list of the missing ghost grains and their diameters by feeding the number of missing ghost grains together with the MicroCT resolution into the grain-size distribution sampling function (available in the repository of Out et al., 2023). Finally, we simulate grains from the list of ghost grains and place them on the honeycomb structure obtained from the MicroCT analysis besides the larger iron-oxide particles that were already detected. Hence, by extracting the honeycomb structure and MicroCT resolution, we are able to simulate a realistic distribution of all iron-oxides in a basaltic sample, with diameters down to the superparamagnetic range.

As an example we consider a hypothetical MicroCT analysis with a resolution of 0.1 μm that produced a honeycomb structure with a surface area of 4 mm^2. Then we would need to populate this honeycomb structure with 9×10^5 particles per mm^2 (dashed line in Fig. 6). This implies that we miss 3.6×10^6 ghost grains in the entire sample with

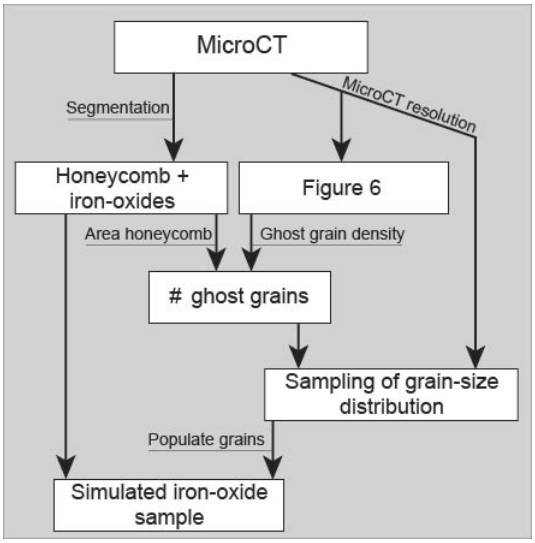

Figure 5. Overview of the protocol to build realistic models of the physical distribution of iron-oxides in a basalt. By segmenting the MicroCT image, we only retain the honeycomb structure and the visible iron-oxides. The MicroCT resolution is required as input for the relation to sample the grain-size distribution of iron-oxides (Fig. 6). Multiplying the ghost grain density with the honeycomb surface area extracted from the MicroCT image, we are able to determine how many grains are left undetected by MicroCT. Given the MicroCT resolution and the number of ghost grains, we sample the grain-size distribution function (see Out et al., 2023) to obtain a list of grain diameters. These grain diameters are used to construct particles that are randomly placed on the extracted honeycomb structure. A graphical overview can be found in the supplementary information (Figure S1).

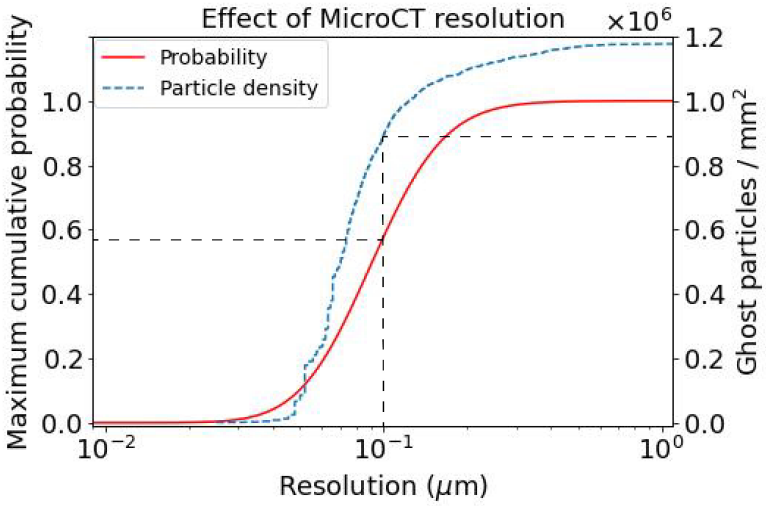

Figure 6. Maximum probability and particles per mm^2 mineral interface area as function of MicroCT resolution. Based on this figure we can determine how many grains have to be sampled from the provided grain-size distribution. By providing the maximum cumulative probability to the grain-size distribution, we can select the maximum grain-size that should be sampled. For example, for 4 mm^2 mineral interface area and a MicroCT resolution of 0.1 μm, we would sample 900.000 particles/mm^2 × 4 mm^2 = 3.6 million particles with a maximum cumulative probability of 0.57. For a resolution larger than 1.0 μm, we would sample 1.20 million grains per mm^2 mineral interface area.

a surface area of 4 mm^2. To obtain the list of grains that we need to add to the honeycomb structure we sample the grain-size distribution 3.6 million times using a maximum cumulative probability of 0.57 (dashed line in Fig. 6) for grains with a diameter between 0 and 0.1 μm. These grains are then randomly placed on the honeycomb structure together next to the larger iron-oxide particles that were already detected with MicroCT.

3.3 Implications for Micromagnetic Tomography

The results of previous MMT based on synthetic samples in which the grain size distribution was controlled (e.g. (most) results in de Groot et al., 2018, 2021)) are most likely not disturbed by ghost grains, because the iron-oxide grains have been sieved for a size larger than the MicroCT resolution. For that reason, their sample mainly consisted of particles larger than 5 μm, which could be easily detected by MicroCT. However, the natural basalt samples used by de Groot et al. (2021) and Kosters et al. (2023) undoubtedly contain undetected ghost grains. Both articles study the magnetic moment of 1,646 iron-oxides detected by MicroCT in a 30 μm thin section of Hawaiian basaltic rock, which is a sister-specimen as subjected to our study. The resolution of the MicroCT used in those studies is $\sim$1 μm and the mineral surface area is $\sim$4 mm^2. According to Fig. 6, this implies the existence of 4.8×10^6 undetected particles, which results in $\sim$3,000 ghost grains per detected iron-oxide.

All of these ghost grains might scramble the signal of the detected iron-oxides leading to erroneous magnetic moments for the detected grains produced by the MMT inversion. Remarkably, both studies do not present unrealistic magnetic moments for the detected iron-oxide particles, and their results are (somewhat) interpretable in terms of magnetic moment and direction. Also, reported trends as function of grain-size and magnetic treatment follow expectations based on earlier work (e.g. Dunlop & Özdemir, 1997). It is therefore likely that, although high in number, the small ghost grains do not have a large enough magnetic moment to have a major contribution to magnetic signal on the surface of the sample. Another possibility is that the spatial resolution of the surface magnetometry data might not be sufficient to locate the weak signal of these ghost particles. As its magnetic moment is highly dependent on the size of a grain (Dunlop & Özdemir, 1997) it is likely that the magnetic moments of larger grains are less affected by ghost grains in an MMT inversion, compared to grains that are just above the detection threshold of the MicroCT analysis used. To characterise the reliability of MMT results as func-

tion of grain size, a future study that models the impact of the undetected ghost grains on MMT results is critical.

4 Conclusions

Here we produced a grain-size distribution of all iron-oxides larger than the superparamagnetic threshold in an Hawaiian basalt by combining MicroCT and FIB-SEM data of sister-specimens. The MicroCT and FIB-SEM datasets could not be combined one-to-one due to volume difference, so they were scaled using the interface area of large, non-iron-oxide, minerals present in the sample (i.e. honeycomb structure), because iron-oxides tend to cluster on the edges of large minerals. Through this scaling procedure we have created a lognormal-like distribution between 20 nm to 10 μm that spans the range of SD, PSD, and MD iron-oxides. This distribution is probably a slight overestimation of the concentration of iron-oxide grains, caused by the choice of FIB-SEM study area with relatively many iron-oxides. This grain-size distribution can be used to populate realistic models of the physical distribution of iron-oxides in a sample; and makes it possible to assess the impact of undetected ghost grains on micromagnetic and MMT studies. Due to the high demands of both MicroCT and FIB-SEM analyses we could only process one sample from a well-characterised Hawaiian lava flow in this study. Future studies can build on our theory of combining FIB-SEM and MicroCT data through the surface area of the honeycomb structure of larger minerals produced by the MicroCT analysis to study other sample material as well.

Data availability statement

The FIB-SEM, MicroCT, and SEM data used for obtaining and verifying, and the jupyter notebooks employed for generating the grain-size distribution and honeycomb structure in this study are available at YODA via https://doi.org/10.24416/UU01-QNASXB with a CC-BY-NC-4.0 license (Out et al., 2023). Numerical calculations were executed with support of NumPy (Harris et al., 2020), SciPy (Virtanen et al., 2020), OpenCV (Bradski, 2000), and Matplotlib (Hunter, 2007) Python libraries. The MicroCT analysis for this study was generated using Dragonfly software, Version 2022.1.0.1259 for Windows. Object Research Systems (ORS) Inc, Montreal, Canada, 2022.

Acknowledgments

This project has received funding from the European Research Council (ERC) under the European Union's Horizon 2020 research and innovation program (Grant agreement No. 851460 to L.V. de Groot). This publication results from work carried out under transnational access action under the support of EXCITE – EC- HORIZON 2020 – INFRAIA 2020 Integrating Activities for Starting Communities (Grant agreement No. 101005611).

References

Berndt, T., Muxworthy, A. R., & Fabian, K. (2016). Does size matter? statistical limits of paleomagnetic field reconstruction from small rock specimens. *Journal of Geophysical Research: Solid Earth*, *121*(1), 15–26.

Bradski, G. (2000). The OpenCV Library. *Dr. Dobb's Journal of Software Tools*.

de Groot, L. V., Biggin, A. J., Dekkers, M. J., Langereis, C. G., & Herrero-Bervera, E. (2013, 12). Rapid regional perturbations to the recent global geomagnetic decay revealed by a new Hawaiian record. *Nature Communications*, *4*(1), 2727. Retrieved from `www.nature.com/naturecommunicationshttp://www.nature.com/articles/ncomms3727` doi: 10.1038/ncomms3727

De Groot, L. V., Fabian, K., Bakelaar, I. A., & Dekkers, M. J. (2014). Magnetic force microscopy reveals meta-stable magnetic domain states that prevent reliable absolute palaeointensity experiments. *Nature Communications*, *5*(1), 4548.

de Groot, L. V., Fabian, K., Béguin, A., Kosters, M. E., Cortés-Ortuño, D., Fu, R. R., ... Barnhoorn, A. (2021). Micromagnetic tomography for paleomagnetism and rock-magnetism. *Journal of Geophysical Research: Solid Earth*, *126*(10), e2021JB022364.

de Groot, L. V., Fabian, K., Béguin, A., Reith, P., Barnhoorn, A., & Hilgenkamp, H. (2018). Determining individual particle magnetizations in assemblages of micrograins. *Geophysical Research Letters*, *45*(7), 2995–3000.

Dunlop, D. J., & Özdemir, Ö. (1997). *Rock Magnetism*. Cambridge University Press. Retrieved from `https://www.cambridge.org/core/product/identifier/9780511612794/type/book` doi: 10.1017/cbo9780511612794

Einsle, J. F., Harrison, R. J., Kasama, T., Conbhuí, P. Ó., Fabian, K., Williams, W., ... Midgley, P. A. (2016). Multi-scale three-dimensional charac-

terization of iron particles in dusty olivine: Implications for paleomagnetism of chondritic meteorites. *American Mineralogist*, *101*(9), 2070–2084. Retrieved from https://doi.org/10.2138/am-2016-5738CCBY doi: doi:10.2138/am-2016-5738CCBY

Fabian, K., & De Groot, L. V. (2019, 2). A uniqueness theorem for tomography-assisted potential-field inversion. *Geophysical Journal International*, *216*(2), 760–766. Retrieved from http://arxiv.org/abs/1712.06136https://academic.oup.com/gji/article/216/2/760/5151336 doi: 10.1093/gji/ggy455

Glenn, D. R., Fu, R. R., Kehayias, P., Le Sage, D., Lima, E. A., Weiss, B. P., & Walsworth, R. L. (2017, 8). Micrometer-scale magnetic imaging of geological samples using a quantum diamond microscope. *Geochemistry, Geophysics, Geosystems*, *18*(8), 3254–3267. Retrieved from https://onlinelibrary.wiley.com/doi/abs/10.1002/2017GC006946 doi: 10.1002/2017GC006946

Harris, C. R., Millman, K. J., van der Walt, S. J., Gommers, R., Virtanen, P., Cournapeau, D., ... Oliphant, T. E. (2020, 9). Array programming with NumPy. *Nature*, *585*(7825), 357–362. Retrieved from http://www.nature.com/articles/s41586-020-2649-2 doi: 10.1038/s41586-020-2649-2

Hunter, J. D. (2007, 5). Matplotlib: A 2D Graphics Environment. *Computing in Science & Engineering*, *9*(3), 90–95. Retrieved from http://nipy.scipy.http://ieeexplore.ieee.org/document/4160265/ doi: 10.1109/MCSE.2007.55

Kosters, M. E., de Boer, R. A., Out, F., Cortés-Ortuño, D. I., & de Groot, L. V. (2023). Unraveling the magnetic signal of individual grains in a hawaiian lava using micromagnetic tomography. *Geochemistry, Geophysics, Geosystems*, *24*(4), e2022GC010462. Retrieved from https://agupubs.onlinelibrary.wiley.com/doi/abs/10.1029/2022GC010462 (e2022GC010462 2022GC010462) doi: https://doi.org/10.1029/2022GC010462

Lindblad, J. (2005). Surface area estimation of digitized 3d objects using weighted local configurations. *Image and Vision Computing*, *23*(2), 111–122.

Nagy, L., Williams, W., Muxworthy, A. R., Fabian, K., Almeida, T. P., Conbhui, P. O., & Shcherbakov, V. P. (2017). Stability of equidimensional pseudo-single-domain magnetite over billion-year timescales. *Proceedings of the National*

Academy of Sciences of the United States of America, *114*(39), 10356-10360. doi: 10.1073/pnas.1708344114

Néel, L. (1955, 4). Some theoretical aspects of rock-magnetism. *Advances in Physics*, *4*(14), 191–243. Retrieved from https://www.tandfonline.com/doi/abs/10.1080/00018735500101204http://www.tandfonline.com/doi/abs/10.1080/00018735500101204 doi: 10.1080/00018735500101204

Nikolaisen, E. S., Harrison, R. J., Fabian, K., & McEnroe, S. A. (2020). Hysteresis of natural magnetite ensembles: Micromagnetics of silicate-hosted magnetite inclusions based on focused-ion-beam nanotomography. *Geochemistry, Geophysics, Geosystems*, *21*(11), e2020GC009389.

Out, F., Cortés-Ortuñno, D., Fabian, K., van Leeuwen, T., & de Groot, L. V. (2022). A first-order statistical exploration of the mathematical limits of micromagnetic tomography. *Geochemistry, Geophysics, Geosystems*. doi: e2021GC010184

Out, F., de Boer, R. A., Walmsley, J., & de Groot, L. V. (2023). *Replication Data for: Modeling the Distribution of Iron-oxides in Basalt by combining FIB-SEM and MicroCT Measurements.* YODA. Retrieved from https://public.yoda.uu.nl/geo/UU01/QNASXB.html doi: 10.24416/UU01-QNASXB

Smirnov, A. (2006). Memory of the magnetic field applied during cooling in the low-temperature phase of magnetite: Grain size dependence. *Journal of Geophysical Research: Solid Earth*, *111*(B12).

Tauxe, L. (2010). *Essentials of paleomagnetism.* Univ of California Press.

Tauxe, L., & Yamazaki, T. (2015). Paleointensities. In *Treatise on geophysics* (pp. 461–509). Elsevier. doi: 10.1016/B978-0-444-53802-4.00107-X

ter Maat, G. W., Pennock, G. M., & de Groot, L. V. (2018). Data descriptor: A chemical, crystallographic and magnetic characterisation of individual iron-oxide grains in Hawaiian lavas. *Scientific Data*, *5*, 1–9. doi: 10.1038/sdata.2018.162

Virtanen, P., Gommers, R., Oliphant, T. E., Haberland, M., Reddy, T., Cournapeau, D., ... van Mulbregt, P. (2020, 3). SciPy 1.0: fundamental algorithms for scientific computing in Python. *Nature Methods*, *17*(3), 261–272. Retrieved from https://doi.org/10.1038/s41592-019-0686-2http://www.nature.com/articles/s41592-019-0686-2 doi: 10.1038/s41592-019-0686-2

512 Yu, Y., Dunlop, D. J., & Özdemir, Ö. (2002). Partial anhysteretic remanent mag-
513 netization in magnetite 1. additivity. *Journal of Geophysical Research: Solid*
514 *Earth*, *107*(B10), EPM–7.

Supporting Information for "Modeling the Distribution of Iron-oxides in Basalt by combining FIB-SEM and MicroCT Measurements"

Frenk Out[1], Rosa A. de Boer[1], John Walmsley[2], Lennart V. de Groot[1]

[1]Paleomagnetic laboratory Fort Hoofddijk, Department of Earth Sciences, Utrecht University, Budapestlaan 17, 3584 CD Utrecht, The Netherlands.

[2]Department of Materials Science & Metallurgy, University of Cambridge, 27 Charles Babbage Road, CB3 0FS Cambridge, United Kingdom.

Contents of this file

1. Figures S1

Corresponding author: F. Out, Paleomagnetic laboratory Fort Hoofddijk, Department of Earth Sciences, Utrecht University, Budapestlaan 17, 3584 CD Utrecht, The Netherlands. (f.out@uu.nl)

1. Graphical overview of building a realistic iron-oxide model

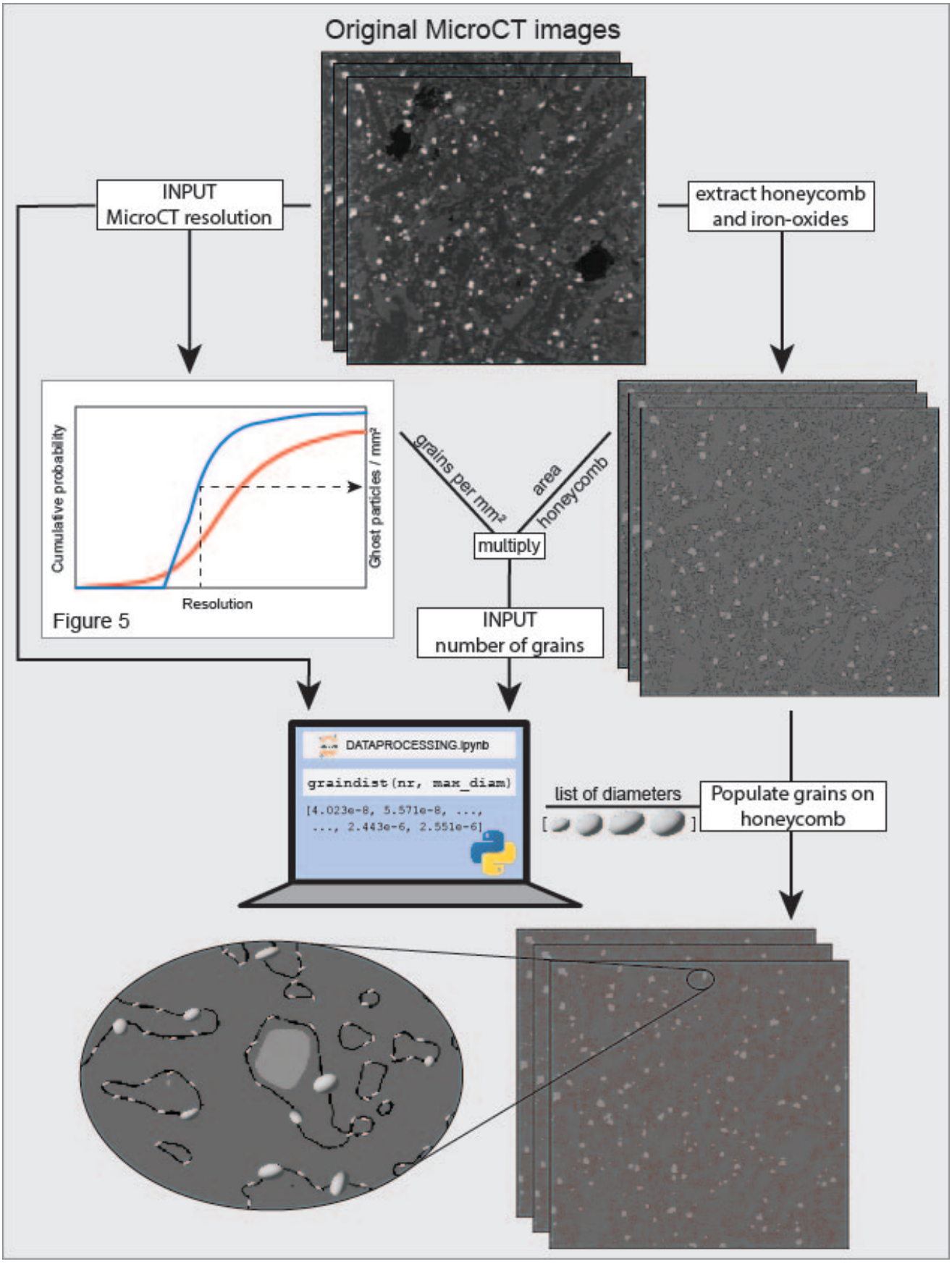

Figure S1. Graphical overview of the protocol to build a realistic iron-oxide model. See section 3.2 of the main text for an explanation of the protocol.